The Proper Motion of the Large Magellanic Cloud Using HST

Nitya Kallivayalil, Roeland P. van der Marel, Charles Alcock, Tim Axelrod, Kem Cook , A. J. Drake, M. Geha

August 19, 2005

Disclaimer

LAWRENCE
LIVERMORE
NATIONAL
LABORATORY

The Proper Motion of the Large Magellanic Cloud Using HST

Nitya Kallivayalil, Roeland P. van der Marel, Charles Alcock, Tim Axelrod, Kem Cook , A. J. Drake, M. Geha

August 19, 2005

Disclaimer

The Proper Motion of the Large Magellanic Cloud using *HST*

Nitya Kallivayalil[1]

Harvard-Smithsonian Center for Astrophysics, 60 Garden Street, Cambridge, MA 02138

Roeland P. van der Marel[2]

Space Telescope Science Institute, 3700 San Martin Drive, Baltimore, MD 21218

Charles Alcock[3]

Harvard-Smithsonian Center for Astrophysics, 60 Garden Street, Cambridge, MA 02138

Tim Axelrod[4]

Steward Observatory, University of Arizona, Tucson, AZ 85721

Kem Cook[5]

Lawrence Livermore National Laboratory, University of California, P.O. Box 808, L-413, Livermore, CA 94551

A. J. Drake[6]

Caltech, CACR, MC 158-79, 1200 E. California Blvd, CA 91125

and

M. Geha[7,8]

The Observatories of the Carnegie Institute of Washington, 813 Santa Barbara Street, Pasadena, CA 91101

---

[1]nkalliva@cfa.harvard.edu

[2]marel@stsci.edu

[3]calcock@cfa.harvard.edu

[4]taxelrod@as.arizona.edu

[5]kcook@guen.ucllnl.org

[6]ajd@cacr.caltech.edu

ABSTRACT

We present a measurement of the systemic proper motion of the Large Magellanic Cloud (LMC) from astrometry with the High Resolution Camera (HRC) of the Advanced Camera for Surveys (ACS) on the Hubble Space Telescope (*HST*). We observed LMC fields centered on 21 background QSOs that were discovered from their optical variability in the MACHO database. The QSOs are distributed homogeneously behind the central few degrees of the LMC. With 2 epochs of HRC data and a ~ 2 year baseline we determine the proper motion of the LMC to better than 5% accuracy: $\mu_W = -2.03 \pm 0.08$ mas yr^{-1}, $\mu_N = 0.44 \pm 0.05$ mas yr^{-1}. This is the most accurate proper motion measurement for any Milky Way satellite thus far. When combined with HI data from the Magellanic Stream this should provide new constraints on both the mass distribution of the Galactic Halo and models of the Stream.

Subject headings: Magellanic Clouds

1. Introduction

The Magellanic Clouds (MCs) are the closest, easily observable galaxies from our vantage point in the Milky Way. They are of fundamental importance for studies of stellar populations, the interstellar medium, and the cosmological distance scale. Moreover, due to their locations at 50 kpc (LMC) and 61 kpc (SMC) from the sun, and ~ 25 kpc from the Galactic Plane, they provide one of our best probes of the composition and properties of the Galactic dark halo. Precise measurements for the proper motions (PMs) of the Magellanic Clouds combined with observational knowledge of the distribution and velocities of HI gas in the Magellanic Stream can constrain models of the shape and radial density distribution of the Galactic dark halo as well as theoretical models for the formation of the Magellanic Stream.

Few developments in modern astronomy are as important as the discovery of cosmic dark matter. Most of the matter in the Universe is invisible to astronomers. In the Milky Way, the dark component is about twenty times more massive than the visible disk of stars and gas. The dark matter forms a vast, diffuse halo that occupies more than a thousand times

[7]mgeha@ociw.edu

[8]Hubble Fellow

the volume of the stellar disk. The composition of this dark halo is unknown, but it may comprise a mixture of ancient degenerate dwarf stars and exotic, hypothetical elementary particles (for a review see Alcock 2000).

The investigation of the Galactic halo is complicated by our immersion deep inside it. Interior to the Solar circle the rotation curve may be measured with confidence (see e.g. Fich & Tremaine 1991). While the estimates out to 20 kpc are not as robust, these observations indicate that the rotation curve is flat (Merrifield 1992; Yoshiaki & Rubin 2001). Much has been learned about the halo in the direction out of the plane from the study of the motions of gas clouds and stars. These imply that the halo is more spherical than disk-like, but no precise measurement for its axial ratio exists (van der Marel 2001). Analyses of the kinematics of some globular clusters and small satellite galaxies suggest that the halo extends out to ∼ 200 kpc (e.g., Wilkinson & Evans 1999). For the large majority of these objects there is only radial velocity data, and where available, proper motions are much less precisely determined than the radial velocities. So while these studies constrain the total halo mass, they say little about its shape or distribution. Spherical symmetry and a particular density distribution are generally *assumed*.

The Magellanic Stream is an HI emission feature that spans more than 100° across the sky (Brüns et al. 2005). It consists of gas that trails the Magellanic Clouds as they orbit the Milky Way and provides an opportunity for detailed study of tidal disruption of galaxies as well as the Milky Way dark halo. Many detailed theoretical models have been constructed for the Magellanic Stream (Gardiner & Noguchi 1996; Lin, Jones & Klemola 1995; Heller & Rohlfs 1994). These models describe how the Magellanic Clouds orbit the Milky Way, and how they lose material through tidal effects and other physical mechanisms. The model parameters are adjusted to best reproduce the observed density, morphology and velocities of the HI gas seen along the Magellanic Stream. The most sophisticated calculations in the class of models that invoke tidal stripping are those by Gardiner & Noguchi (1996). In their models the LMC and SMC form a gravitationally bound system that orbits the Milky Way. The Magellanic Stream represents material that was stripped from the SMC ∼ 1.5 Gyr ago. This was the time of the previous perigalactic passage, which coincided with a close encounter between the Clouds.

In Magellanic Stream models, the orbit of the clouds is one of the prime variables that is adjusted to fit the data. As a result of Newton's Law, the orbit is fully determined by: (a) the position of the Clouds on the sky; (b) the present distance of the Clouds from the sun; (c) the radial velocities of the Clouds; (d) the proper motions of the Clouds; and (e) the gravitational potential of the Galactic dark halo. The first three of these are known relatively well; the latter two are not. Even small differences in the proper motions can give vastly

different orbits for the Clouds, especially when considered over the long period of time over which the Magellanic Stream developed. The usual approach has therefore been to estimate the proper motions of the Clouds from the properties of the Magellanic Stream, assuming a fixed Galactic halo gravitational potential (usually a simple spherical isothermal halo). The results imply that the Magellanic Clouds are just past their pericenter (itself at ~ 45 kpc from the Galactic Center), that the apocenter to pericenter ratio is $\sim 2.5 : 1$, and the orbital period is ~ 1.5 Gyr. The inferred tangential velocity in the Galactocentric rest-frame has differed substantially from model to model, ranging from, e.g., $v_{\rm LMC,tan} = 352$ km/s (Heller & Rohlfs 1994) to 285 km/s (Gardiner & Noguchi 1996).

It was realized by Heller & Rohlfs (1994) and Lin, Jones & Klemola (1995) that the arguments used to model the Magellanic Stream can be turned around. If the proper motions of the Magellanic Clouds are known, then the gravitational potential of the Galactic dark halo can be determined from models of the Magellanic Stream. They explored this using the available proper motion data, but found that its accuracy was insufficient to obtain strong constraints on the dark halo properties. Kroupa et al. (1994) found that a proper motion better than 0.1 mas yr^{-1} is required for strong results.

So far the proper motion of the LMC has not been known accurately enough to strongly constrain properties of the Milky Way dark halo. Measurements, however, are steadily improving and determinations are available from the following sources: Kroupa et al. (1994), using stars from the PPM Catalogue; Jones et al. (1994), using photographic plates with a 14 year epoch span; Kroupa & Bastian (1997), using Hipparcos data; Drake et al. (2002), using data from the MACHO project; Anguita, Loyola & Pedreros (2000) and Pedreros et al. (2002), using CCD frames with an 11 year epoch span; and Momany & Zaggia (2005), using the USNO CCD Astrograph all-sky Catalog (UCAC2). The measurements are all consistent with each other to within the error bars with the exception of two outliers: Anguita et al. (2000) and Momany & Zaggia (2005) present values of $(\mu_{RA}, \mu_{DEC}) \sim (+0.84, +4.32)$ mas yr^{-1}. When these two results are ignored, the weighted average of the remaining measurements yields proper motions towards the West and North of $(\mu_W, \mu_N) = (-1.68 \pm 0.16, 0.34 \pm 0.16)$ mas yr^{-1} (Van der Marel et al. 2002) i.e. to $\sim 13\%$ accuracy. This implies $v_{\rm LMC,tan} = 281 \pm 41$ km/s, which is consistent with most of the published Magellanic Stream models, but is not accurate enough to discriminate between them. The proper motion of the SMC is much less well known than that of the LMC, and only one reasonably accurate measurement exists. Kroupa & Bastian (1997) obtain a value of $(\mu_\alpha cos(\delta), \mu_\delta) = (1.23, -1.21)$ mas yr^{-1} for the SMC with an error of $(0.84, 0.75)$ mas yr^{-1}.

A sound measurement of the proper motion of the LMC requires all of the following key factors: (1) an instrument which can perform the astrometry with adequate precision;

(2) a reference frame consisting of point sources, such as quasars, distributed widely behind the Clouds; (3) secure determination of the membership of stars in the LMC; and (4) a reliable kinematic model of the internal rotation of the Clouds. The previous estimates of the motions (referred to above) do not satisfy all of these requirements. However, a much improved measurement is now possible. Some teams have identified QSOs behind our neighboring galaxies in order to provide good inertial reference frames against which the motions of these galaxies can be measured (Geha et al. 2003; Dobrzycki et al. 2002; 2003); the *HST* has been shown to be very stable for astrometry (Anderson & King 2003) and in particular the Advanced Camera for Surveys (ACS) has higher resolution, and is better calibrated and more stable than even WFPC2 (Anderson & King 2004; hereafter AK04).

We were awarded two epochs on the High Resolution Camera (HRC) on the ACS in Cycle 11 and Cycle 13 for a study of the proper motions of the MCs. We report our proper motion result for the LMC in this paper. SMC results as well as implications for the MC system as a whole will be presented in subsequent papers. The paper is outlined as follows: §2 deals with the sample and the observations; §3 describes our analysis; §4 presents the center of mass proper motion of the LMC; §5 is a discussion and §6 is a summary.

2. Sample Selection and Description of Observations

2.1. Sample

A total of 54 QSOs were identified behind the Magellanic Clouds from their optical variability in the MACHO database (Geha et al. 2003). Out of this sample, 44 QSOs were behind the LMC. In our first epoch program (GO-9462; Cycle 11), we proposed to image fields around these QSOs with ACS/HRC in snapshot mode. In a snapshot proposal the targets are randomly selected from the proposed list, but with manually assigned priorities. We successfully observed 34 of the 44 LMC QSOs in the first epoch. In the second epoch program GO-10130 (Cycle 13) we re-imaged the targets that were observed in epoch 1 and for maximally efficient use of *HST* resources we again chose to observe in snapshot mode. We achieved a completion rate of 62% for epoch 2 and 48% overall, so that our final sample consists of 21 targets. Table 1 describes this sample. It lists the ID number for each QSO (each QSO field will be referred to by its ID number subsequently), as well as its MACHO ID (for referencing purposes with Geha et al. 2003), RA, DEC (J2000), *V* magnitude (an average of our measurements from both epochs) and redshift. Table 1 also lists the execution date, visit number, exposure time and orientation for each epoch's observations, as well as the time baseline that was ultimately achieved for each target. These are discussed in §2.2.

Figure 1 is a plot of the QSOs behind the LMC. QSOs for which we obtained two epochs of data are marked with white circles. Their distribution behind the LMC is reasonably uniform. QSOs which did not make it through one or both of our snapshot programs are marked with white squares.

2.2. Scheduling and Execution

In a snapshot program the targets are executed in the cycle so as to fill gaps in the HST schedule. The majority of our observations were scheduled in the first part of the cycle. It is interesting to study some of the specifics of the scheduling times and the quantities that they affect. Figure 2(a) is a histogram of the time baseline for each QSO field (in years). The median baseline that we achieved is ~ 1.9 years but there is a spread from ~ 1.1 to 2.7 years. For observations with HST, the date of observation determines the orientation of the detector with respect to the sky (see the HST Primer, Karakla 2005). Again, because of the snapshot nature of our project, the orientations were not fixed *a priori* and hence were not identical from one epoch to the next. Figure 2(b) is a histogram of the orientations on the sky (ORIENTAT) of each of our QSO fields for both epochs (ORIENTAT is defined as the angle on the sky, East of North, of the detector y-axis). Figure 2(c) is a histogram of the relative telescope rotation between the epochs for each QSO field, plotted between -180°and 180° . It shows that the observations were not taken at completely random orientations, for there is a broad peak near $\sim 0°$. Nonetheless, there is considerable randomness in the orientation of the telescope with respect to the sky, both in an absolute and in a relative sense. This is good because it implies that any possible systematic proper motion errors tied to the CCD frame will average to zero roughly as $1/\sqrt{N}$. The possibility of actual systematic effects are investigated in detail in §3.3.

Our observing strategy involved the use of the HRC because it provides the highest resolution available (the average pixel scale is 28.27 mas/pixel - see AK04) and is well calibrated for astrometry. It is also well sampled even in the bluest filters and thus a star's integrated flux does not depend strongly on where it lands in a pixel. It is optimized towards the visual and red part of the spectrum and so for our main astrometry goals we chose the F606W filter which is a broad V filter with high throughput. This filter is also not too red and thus avoids possible issues with the HRC red halo at wavelengths $\gg 7000$Å (see the ACS Instrument Handbook, Pavlovksy et al. 2005). In addition to F606W, we used F814W which is a broad I filter for imaging in the first epoch only, not for the main astrometry, but to be able to place sources on a color-magnitude diagram (CMD). We thought that this might help assist in the rejection of foreground stars.

For the F606W filter, in epoch 1, exposure times were chosen so as to achieve a S/N of at least 100 for the QSOs based on the known MACHO magnitudes. In epoch 2 the exposure times were chosen to be somewhat larger than in epoch 1 to take into account the fact that the MACHO sources were considerably blended and that the actual V magnitudes measured from first epoch HST data tended to be dimmer than the MACHO magnitudes. Some of the isolated QSOs actually turned out to be brighter because of their intrinsic variability. Note that on the timescale of our proper motion measurements, the expected photometric variability is only approximately a few tenths of a magnitude in the V-band and so we quote an average from both epochs in Table 1. For the F814W filter, the exposure time was set to 1.7 minutes total which is sufficient for photometry.

We chose the same dither pattern in the F606W filter for both epochs. This amounted to 8 exposures per epoch for each QSO (16 exposures total for both epochs) taken using two four-point half-pixel shifts which were shifted relatively by an integer 8-pixel amount. Figure 3 is a schematic of this dither pattern. Since we did not plan to do astrometry with the F814W images we chose a simple CR-SPLIT in order to be able to reject cosmic rays and other transients. In summary, each QSO field has 18 images associated with it - 16 in V-band and 2 in I-band - and each of the V-band images were dithered to minimize any pixel-location based systematic errors.

For our basic reduction purposes we used the bias-subtracted, dark-subtracted, flat-fielded images (_flt.fits) provided by the STScI/ACS data reduction pipeline. AK04 found that these images are well-behaved for astrometric purposes. They are not, however, corrected for geometric distortion. We did not use the geometrically corrected products created by the MultiDrizzle software (_drz.fits) since they involve a re-sampling that might degrade the astrometry. Instead of geometrically correcting the images, we geometrically corrected the star positions on the images, after doing PSF-fitting, as we will discuss in §3 below.

3.   Analysis

3.1.   Methodology for PSF-fitting and Distortion Solution

The HRC has a large amount of geometric distortion due to its off-axis location and it is necessary to understand this fully because a high-precision astrometric program such as ours requires a distortion solution that is at least as accurate as the centroiding. Although the distortion is large, it is very stable, and can therefore be calibrated accurately. This calibration has been done by AK04, and our analysis relies heavily on their work. They and Krist (2003) have shown that for ACS/HRC the Point Spread Function (PSF) doesn't vary

significantly over the field (in contrast to WFPC2). Although the *HST* PSF does vary with time due to "breathing" (thermal effects associated with day/night transitions) and long-term changes in focus, these changes affect mostly the relative amounts of light in the core and the wings of the PSF. The actual shape of the core is not altered significantly. AK04 developed multi-filter PSFs for the HRC using a large dataset of 40 observations each with 20 different pointings of the globular cluster 47 Tuc (*HST* Calibration Programs GO-9028, GO-9443 & GO-9019).

AK04 also developed a detailed solution to the geometric distortion which they modeled as the combination of a large-scale distortion characterized by a fourth-order polynomial and fine-scale variations characterized by a look-up table that can be linearly interpolated to give the adjustment required at any point in the image. They showed that the second and higher order terms are stable over short and long timescales. However, the linear terms vary with time (even within a single *HST* orbit) due to breathing, differential velocity aberration, and other effects. Therefore any two exposures must be brought to a common frame with the use of a 6 parameter linear transformation (the 6 parameters are scale, skew, translation and rotation). When this is done, the geometric distortion correction is accurate and stable over long timescales to ∼0.005 pixel. For comparison, given our median time baseline (see Figure 2), the proper motion of the LMC, estimated on the basis of previous work (Van der Marel et al. 2002), corresponds to a position difference of 0.1 pixels between epoch 1 and 2. Thus we have a very good handle on systematics in this regard.

To sum up, AK04 have provided software that finds the point sources on an image, fits the PSF to determine the raw stellar position and flux, applies a distortion correction to calculate the geometrically corrected stellar position (i.e., on a frame that is locally Cartesian on the sky) and finally, applies a photometric correction to the sources for geometric distortion and finite aperture effects.

3.2. Data Analysis

We ran the AK04 code on all 18 images for each field. At this stage, some cuts were made based on crowding (by specifying how far away the next brightest source can be) and threshold (by specifying the minimum peak brightness in excess of the sky background). These cuts were not stringent so as to identify the largest possible number of real sources. Using the first V-band image in the first epoch as a reference, we cross-identified the detected sources in all other images with it. We then created a master-list of sources for each QSO field by accepting only those sources detected in all 18 images and for which the magnitudes in all V images were in mutual agreement to within 6σ. This rejected all cosmic rays, other

transients and bad pixels that were detected as sources (note that individual exposures were short so that cosmic ray rejection would be reliable). This also rejected all bona fide stars that had fallen off the field in just a few of the images because of the dither pattern or the CCD rotation between epochs 1 & 2, and stars in which one or more of the measurements were sub-optimal. So in this respect this cut was conservative. However, it ensured that we used exactly the same subset of stars for every image in every epoch, which in turn minimized any potential for systematic differences and errors. Table 2 lists for each field the number of real sources (detected in at least half of the images) and the number of sources in the master-list (detected in every image in every epoch with magnitudes consistent to within 6σ). As can be seen from the table, this generally cuts down the number of sources by a factor of two.

We obtained an average V and I magnitude and photometric errors for each source in the master-list by combining the measurements of the individual exposures. For each field we identified the QSO in the master-list from registering with the MACHO discovery images (see Geha et al. 2003). We then removed the QSO from the master-list to obtain a list that consisted primarily of LMC objects. We were not interested in measuring (nor were we able to measure) the relative motion of LMC stars within a given field with respect to each other. We could only measure the average motion of all the stars in a given field with respect to the QSO. To do this we determined and applied geometric transformations to align the star positions in every image with those of the reference image. Then subsequently, we used the same transformations to correct the position of the QSO. The motion of the QSO, over the time baseline, was then obtained simply as the difference between its average position in each epoch. Since in reality the QSO is so distant that it is essentially fixed on the sky, the resulting measurement is just the reflex motion due to the average motion of LMC stars.

We used a six parameter linear fit to transform the star positions and align them as best as possible (in a χ^2 sense) with the positions of the same stars in the reference image. We ran the linear transformations iteratively and accepted for use in the calculation of the transformation only those stars for which the proper motion (PM) and the error in the proper motion (δPM), measured relative to the average of the other stars, were both < 0.1 pixels. This rejected foreground stars (in general those are expected to move by $\sim$ 8 mas yr^{-1} towards the North; see Momany & Zaggia 2005) and stars with large centroiding errors. The latter are generally faint stars that were unlikely to improve the accuracy of the result. The terms in the transformations were modified iteratively until the number of stars used in the fit was unchanging.

After determination of the linear transformations for all images, we calculated the PM and δPM for all sources in the master-list, as well as for the QSO. Figure 4 is a schematic

illustrating the basic steps involved in getting a QSO PM in pixels. One component of the final astrometric error is how well we are able to align the stars between epochs. We therefore determined the PM of each star individually as the difference between its average positions in epoch 2 and 1 (just as we do for the QSO). We then ran some statistics to calculate the error in the average PM of all the stars, which we called $\sigma_{\langle PM \rangle}$ (the average itself is zero by definition). This error quantifies how accurately we were able to align the star-fields between the two epochs and gives us an idea of our systematic errors. Table 2 lists the final number of sources (N_{used}) used in the linear transformations for each field. Once the images are aligned the relative motion of the QSO and the star-field is simply the difference in the average position of the QSO from epoch 1 to epoch 2. We called the random error in this difference δPM_{QSO}. The final error in the relative motion between the QSO and the star-field is then $\sqrt{\delta PM_{\text{QSO}}^2 + \sigma_{\langle PM \rangle}^2}$. Figure 5 shows the distribution and contributions of these two components of the final error. δPM_{QSO} is plotted on the x-axis and $\sigma_{\langle PM \rangle}$ is on the y-axis. The straight line marks $\delta PM_{\text{QSO}} = \sigma_{\langle PM \rangle}$. The figure shows that our final errors are dominated by the centroiding errors of the QSO and that the error introduced by aligning the star-field is smaller.

We transformed the results to a PM and δPM of LMC stars in the directions North and West in mas yr^{-1} using the orientation of the reference image with respect to the sky (ORIENTAT), the time baseline, and the fact that the PM of the LMC is the opposite of what we measure for the QSO (technically what we measure is the reflex motion of the QSO). Absolute orientations of HST observations are fairly accurate ($\lesssim 0.003\,°$) and any uncertainty in ORIENTAT has no effect on our final PM errors. Table 2 tabulates the PM for each field and the corresponding error (columns 5 - 8).

3.3. Inspection and Consistency Checks

Figure 6 shows the ($V - I$, V) CMD for the LMC. The QSOs are marked in green and the stars with PM & $\delta PM < 0.1$ pixels are marked in red. The CMD looks consistent with other CMDs of the LMC (see for e.g. Alcock et al. 2000b). The main sequence and the giant branch are clearly visible, and the red clump (which is often used as a distance indicator) is also where we would expect it to be, at $\sim V = 19.1$, $V - I \sim 1$ (see Smecker-Hane et al. 2002). We believed that we might make some additional cuts for a foreground population of stars based on this CMD, but such a population is not clearly delineated, and any cuts we could make (like the very red, dim tail of objects) seem to be obviated by the PM cuts that we employ.

To test the robustness of our results we tried a number of different variations and cuts in

our analysis. Apart from the cuts in PM space to eliminate foreground stars and stars with large centroiding errors, these variations included: a) constraints on the distance of a star from the center of the field (i.e. eliminating stars in the outer edges from our analysis in case the geometric distortion is more complicated than understood in those regions); b) inclusion of higher order terms in the transformation to account for any possible time-variations in the distortion terms; c) making both steeper and looser cuts in the PM and δPM space of the stars (e.g. PM and δPM < 0.05 and 0.2 pixel); d) using only those stars whose PM/δPM $\leq$ 2.5 to further ensure that the transformations are not unduly influenced by stars whose PMs are not statistically consistent with zero. None of these cuts were found to significantly alter the results. In particular they did not affect the fields that could be seen as 'outliers' at that point in the analysis.

Figure 7(a) & (b) show PM and δPM in pixels as a function of V magnitude for all stars in all master-lists of all fields respectively. These plots look reasonable and have the expected shapes with errors $\propto$ (S/N)$^{-1}$. Figure 7(c) shows δPM vs. PM for all stars in all master-lists. It illustrates that the PM residuals are not much larger than the expected random errors.

Figure 8 shows PM vectors for all the stars in all master-lists of all fields in x and y-space in pixels, magnified by a factor of hundred. This enables us to inspect how and if the shifts vary with position on the chip and if there are any other systematic trends in the transformations. All vectors appear to be random both in magnitude and orientation across the field. Figure 9 seeks to address the same concerns, but plots the PMs for the stars with PM and δPM < 0.1 pixels versus x and y position on the chip separately. The scatter in x and y look comparable and there is no obvious trend with position on the chip. Figure 10 is again a plot of PM vs. x and y for the stars, but now the PM values have been binned for every 100 pixels, and the average PM value for each bin is plotted. This allows us to really get down into the noise and investigate systematic errors at the level of a hundredth of a pixel. We conclude from this plot that there is no evidence for systematic errors in the geometric distortion correction larger than $\sim$ 0.005 pixels, which is consistent with the findings of AK04. Thus, all the results look sensible, robust, and well behaved to within the expected accuracy.

4. Proper Motion results

4.1. Field Dependence of Proper Motions

One way to estimate the proper motion of the LMC center of mass is just to average the results from the 21 fields listed in Table 2. However, this is not the most accurate approach. The fields are separated by several degrees and this causes real variations in the PMs of LMC stars in different fields. In general, the motion observed for an individual QSO field can be written as

$$PM(\text{field}) = PM(\text{CM}) + PM_{\text{res}}(\text{field}). \tag{1}$$

Here $PM(\text{CM})$ is the proper motion of the LMC center of mass and $PM_{\text{res}}(\text{field})$ is the field-dependent residual. The latter contains contributions from different effects:

(a) variations as a function of position in the components of the three-dimensional velocity vector of the center of mass that are seen in the plane of the sky ("viewing perspective");

(b) the internal rotation of the LMC;

(c) time variations di/dt and $d\Theta/dt$ in the LMC viewing angles.

The formulae for these contributions can be found in van der Marel et al. (2002, hereafter vdM02). With the help of a model for these contributions one can use the observed proper motion $PM(\text{field})$ for any given field to obtain an estimate $PM_{\text{est}}(\text{CM})$ for the proper motion of the LMC center of mass using

$$PM_{\text{est}}(\text{CM}) \equiv PM(\text{field}) - PM_{\text{res}}(\text{field}). \tag{2}$$

The estimates $PM_{\text{est}}(\text{CM})$ for all fields are listed in Table 2 (columns 9 & 10). The field-dependent correction terms $PM_{\text{res}}(\text{field})$ are small compared to the overall LMC proper motion, but are significant given the accuracy that we are trying to achieve. The average two-dimensional size of the correction terms is 0.20 mas yr^{-1} and the maximum over all fields is 0.53 mas yr^{-1} . The corrections are smaller for fields that are closer to the center of the LMC. The largest contribution to the corrections comes from the viewing perspective effect, which contributes on average 0.15 mas yr^{-1}, with a maximum over all fields of 0.31 mas yr^{-1}. By contrast, the internal rotation contributes on average 0.06 mas yr^{-1} , with a maximum over all fields of 0.20 mas yr^{-1} .

We used an iterative procedure to evaluate equation (2). This is necessary because the residuals $PM_{\text{res}}(\text{field})$ themselves depend either directly or indirectly on the proper motion of the LMC center of mass. At each iteration step we averaged the estimates $PM_{\text{est}}(\text{CM})$ for

– 13 –

the different fields to obtain an optimal estimate for PM(CM). This value was then used in the next iteration step to evaluate the residuals PM_{res}(field). For the internal rotation model of the LMC we fitted the line-of-sight velocity data for 1041 carbon stars (at each iteration step) as in vdM02. This fit depends on the proper motion of the LMC center of mass, because the latter introduces a spurious solid-body component in the observed line-of-sight velocities that must be subtracted while modeling the internal rotation. We did not include any time-dependence of the viewing angles (indicative of precession and nutation of the LMC disk plane) in the model. As we show in §4.4 below, the available observational constraints are consistent with $di/dt = d\Theta/dt = 0$. Where necessary, in the model for PM_{res}(field) we used: distance modulus $m - M = 18.50$, systemic line-of-sight velocity $v_{\text{sys}} = 262.2$ km s^{-1}, center position $\alpha_{\text{CM}} = 5^{\text{h}}\,27.6^{\text{m}}$ and $\delta_{\text{CM}} = -69.87°$, inclination $i = 34.7°$ and line-of-nodes position angle $\Theta = 129.9°$ as in vdM02.

The field-dependent corrections PM_{res}(field) are more-or-less symmetrical around the LMC center. So the corrections approximately average to zero for a distribution of quasar fields that is symmetric around the LMC center. This is not exactly the case for the fields that we observed, but nonetheless, the fields are reasonably homogeneously distributed around the center (see Figure 1). Therefore, the average of the corrections over all fields is smaller than the individual corrections themselves. Moreover, this average is determined primarily by the geometry of the field distribution. The specific assumptions made about the model of the LMC and its rotation have almost a negligible effect. We have run tests in which we varied the values of the model parameters over ranges that are realistic estimates of the observational uncertainties: 5 km s^{-1} in v_{sys}, 10° in inclination, $120 - 155°$ for the range in line-of-nodes position angle, 0.5° in LMC center position, and 0.1 mag in distance modulus. None of these changes affected our final estimate of the proper motion of the LMC center of mass by more than 0.02 mas yr^{-1}.

4.2. Check for Systematic Errors

The quantities PM_{est}(CM) for each field all provide an independent estimate of the same quantity. For each field we calculated the residual vector μ_{resid} between its value of PM_{est}(CM) and the final estimate of the LMC center of mass proper motion that we derived from these estimates (to be discussed in §4.3 below). The scatter in these residuals provides insight into the observational uncertainties. To address the possibility of systematic trends we show in Figure 11 the size $|\mu_{\text{resid}}|$ of the residuals as a function of the following quantities: the V magnitude of the QSO; $V - I$ of the QSO; the number of stars N_{used} used to align the stars in each field between the two epochs; the quantity χ^2/N_{used} that indicates how well

the stars could be aligned between the epochs; and the distance of the QSO to its nearest neighboring star (without application of cuts to the star-list).

There is a clear systematic effect as a function of χ^2/N_{used}. There is one field (ID L13) that has a much higher value of χ^2/N_{used} than the other fields. This field also happens to have the largest residual μ_{resid}. It also has the nearest neighboring star of all fields (only 9 pixels from the QSO). So it is not clear whether this is the reason for the large μ_{resid} or whether it is the poor accuracy (measured by χ^2/N_{used}) with which the star-field could be aligned. There is also a systematic effect as a function of N_{used}. Fields with a very low value of N_{used} do tend in general to have larger residuals than fields with a high value of N_{used}. This makes sense, since one expects to be able to align the data from the two epochs better if there are more stars in the field, and we certainly do not want to trust the fields in which very few stars were used to determine the linear transformations. Thus, based on these plots we decided to retain for our final estimate of the LMC proper motion only the 13 fields for which $N_{\text{used}} > 16$ and $\chi^2/N_{\text{used}} < 15$. These fields are shown with filled circles in Figure 11 while the rejected fields are shown with open circles. Once we have applied these cuts there are no trends in μ_{resid} for the remaining fields with QSO magnitude, color, or distance to the nearest star. Hence, no additional cuts were applied.

The PM values for all the QSO fields are shown in the (μ_W, μ_N)-plane in Figure 12. They are compared to the residual proper motions of all the LMC stars that were used in the transformations. The stars are shown with open circles and the QSOs with filled ones. Panel (a) shows the observed PM values for all fields. Panel (b) shows the estimates $\text{PM}_{\text{est}}(\text{CM})$ derived from the observed values for the final 13 "high-quality" fields only. The reflex motion of the QSOs clearly separates from the star-fields in both panels. The solid lines in (b) mark the weighted average of the 13 fields (see §4.3, equation (3)).

Figure 13 shows the residual vectors μ_{resid} as a function of field position along with the $1-\sigma$ error bars for each field. Rejected and non-rejected fields are shown with open and filled circles respectively. The thick solid vector anchored by a plus sign shows for comparison the size of the inferred center of mass proper motion of the LMC, at the adopted LMC center. For the high quality fields there is no obvious trend as a function of absolute telescope pointing. Low quality fields that were rejected on the basis of their N_{used} or χ^2/N_{used} do tend to have large residuals and appear to be concentrated mainly in the North-East. This reflects the low stellar density in this region (see Figure 1). On the other hand, the LMC is known to have internal motions and these fields appear to both correspond to the location of the LMC spiral arm (Nikolaev et al. 2004) and show a similar residual trend in direction. By not including these fields we thus risk removing a real and interesting trend from the data. However, given the very low numbers of stars in these fields we do not feel that we can detect

such a trend with confidence. Thus, these fields are not included in our final estimates. Note that if we were to include them, they would not make a statistically significant difference to the bulk motion of the LMC (see §4.3). This is illustrated by the bold dashed line in Figure 13 which is a straight average of all 21 fields (columns 5 & 6 of Table 2).

4.3. Influence of CTE degradation

One possible source of systematic errors in our analysis is the degrading Charge Transfer Efficiency (CTE) of the ACS/HRC CCD. When charge is read out from a CCD pixel, some charge is left behind and released at a later time. This causes sources in an image to show faint tails along the detector y-direction. The impact of imperfect CTE is larger for sources that are further from the read-out amplifier. The impact also increases with time, because the continuing bombardment by cosmic rays in the harsh environment of space increases the number of charge traps in the CCD. The effect of imperfect CTE on photometry has been studied in detail by many authors, and has been quantified for the ACS/HRC by Riess (2003). More recently, some attention has been drawn to the impact of imperfect CTE on astrometry (Bristow, Piatek & Pryor 2005; Piatek et al. 2005). These authors quantified this effect for the STIS instrument on HST in the context of a study of the proper motion of the Ursa Minor dwarf spheroidal galaxy. They found that the inferred reflex PM of the QSO in their STIS field changes by 0.47 mas yr^{-1} due to imperfect CTE.

The ACS/HRC CCD was a flight-spare for the STIS instrument, and its detector properties are similar to those of the STIS CCD. However, the effect of imperfect CTE on our LMC PM should be much less than that found in the STIS Ursa Minor study, for several reasons. First, the ACS/HRC pixels span only ~ 28 mas on the sky, as compared to 50 mas for the STIS CCD. So the same star trail in pixel space will produce an astrometric shift in mas that is smaller by a factor of 1.8. Second, the median observation date of our second epoch LMC data was only 2.5 years after installation of the ACS on HST, as compared to 5.0 years for the last epoch in the STIS Ursa Minor study. If the effect of imperfect CTE on astrometry varies linearly with time since installation (as it does for photometry; Mutchler & Sirianni 2005) then our study should be affected by a factor of 2.0 less. And third, we have observations for $N = 21$ different fields (or $N = 13$ for the "high quality" sample), as compared to only 1 in the STIS Ursa Minor study. Since our fields have more or less random detector orientations on the sky, any CTE induced astrometric shift will average down to zero $\propto N^{-1/2}$. So even if we were to make no allowance for CTE one would not expect our study to be affected by more than ~ 0.04 mas yr^{-1}.

The STIS Ursa Minor study could correct explictly for the astrometric effects of CTE

owing to the existence of a detailed model for the underlying STIS CCD detector physics and charge trap properties (Bristow & Alexov 2002). Such a model does not (yet) exist for the ACS/HRC CCD, and it is therefore not possible to correct our data explictly for imperfect CTE. However, a simple correction can be applied by fitting a shift in the detector y-direction of sources that is linearly proportional to both the y-position on the detector and the time since installation of the instrument in space. This is akin to what Piatek et al. (2005) did for the WFPC2 data that they obtained for Ursa Minor. They had to include this term explictly, because they otherwise allowed only for a translation, rotation and scale change between epochs (i.e., a four-parameter linear fit). Instead, in our study we perform a fully general six-parameter linear fit to align the star-fields from different epochs. Therefore, the type of astrometric shift expected from imperfect CTE is automatically allowed for and fitted to the data. This seems to work well, given that the average PMs of the LMC stars do not show a trend with y-position on the detector (see Figure 10). The only thing that we do not allow for is a variation of the astrometric shift with brightness. Brighter sources are less affected by imperfect CTE than fainter sources. Since the QSO is generally brighter than the average LMC star in the field, there might be a small residual CTE effect in the PM for each field. However, we will estimate the final errors in the LMC PM from the scatter between the PM measurements for different fields. Therefore, any residual systematic errors due to imperfect CTE are explictly accounted for in our final error estimates.

So in summary: (1) even when not modeled at all, imperfect CTE is expected to have at most a small effect on our ACS/HRC results for the LMC PM; (2) our methodology for aligning star fields between epochs allows for a low-order correction of the astrometric shifts due to imperfect CTE; and (3) any residual effects of imperfect CTE are explictly accounted for in our final error estimates.

4.4. Proper Motion of the LMC center of Mass

To obtain our final estimate of the LMC proper motion we took the weighted average of the 13 high-quality fields to obtain

$$\mu_W = -2.03 \pm 0.08 \text{ mas yr}^{-1}, \ \mu_N = 0.44 \pm 0.05 \text{ mas yr}^{-1} \text{ (HST)}. \tag{3}$$

The errors in these numbers are based on the RMS scatter between different fields, divided by $\sqrt{N}$. To be conservative we did not use the weighted average errors $[\sum\{\delta\text{PM(field)}\}^{-2}]^{-1/2}$. These errors have a value of 0.03 mas yr^{-1} to the North and to the West, and are a factor of ~ 2 smaller in the Northward direction and ~ 3 smaller in the Westward direction than the errors in equation (3). The fact that the weighted errors, which are due to pure noise

propagation, are smaller than the errors in equation (3) indicates that there is more scatter in the results from different fields than can be accounted for by random errors alone. This is not entirely unreasonable. An error of 0.07 mas yr^{-1} over a baseline of 1.6 years (our mean) corresponds to 0.004 pixels, and it has not been established that there are no systematic errors in, for example, the geometric distortion, at that level (see Figure 10 and AK04). One possible cause of systematic errors might be variations in the higher order geometric distortion terms with time at the level of thousandths of a pixel or residual astrometric effects due to imperfect CTE. Note that if so, such systematic errors would probably have a fixed orientation with respect to the detector. Since our fields were observed at somewhat random orientations because of the snapshot nature of our program (see Figure 2), such systematic errors would still approximately decrease as $1/\sqrt{N}$ when averaging (as we assumed in getting equation (3)).

It is important to note that our result does not depend sensitively on the details of either the modeling of the field-dependence of the PMs, or the criteria applied to reject lower-quality fields, or the actual statistic applied to obtain the average. A straight unweighted average of the observed proper motions for all 21 fields, as listed in Table 2 (columns 5 & 6), yields $\mu_W = -1.97 \pm 0.09$ mas yr^{-1} , $\mu_N = 0.46 \pm 0.10$ mas yr^{-1} . The median is $(-1.98, 0.43)$ mas yr^{-1} . These estimates are both consistent with the result in equation (3) to within the errors.

4.5. Proper Motion Rotation of the LMC

Our data might in principle allow us to detect the rotation of the LMC in the plane of the sky. To address this we plot in Figure 14(a) the residuals

$$\hat{\mu} = \mathrm{PM(field)} - \mathrm{PM(CM)} - \mathrm{PM_{res}(field)}, \tag{4}$$

where PM(field) is the observed proper motion for a field and PM(CM) is the center-of-mass proper motion from equation (3). The quantity $\mathrm{PM_{res}}$(field) is the residual proper motion as in §4.1, but now includes only the contribution from viewing perspective, and *not* the contribution from internal rotation. The residuals $\hat{\mu}$ are therefore the observational estimates of the internal motions of the LMC. For comparison, we show in Figure 14(b) the internal motions predicted by the model employed in §4.1.

It is clear that the observations are dominated by noise, and rotation is not immediately obvious from visual inspection. On the other hand, some signal can be measured by averaging the results from the individual fields. For each field we determined the unit vectors $\vec{u}_{\parallel}$ and $\vec{u}_{\perp}$ along and perpendicular to the direction of rotation predicted by the model. We determined

the components of the residual vectors $\vec{\hat{\mu}}$ along these unit vectors, which are given by the inner products $\hat{\mu}_{\parallel} = \vec{\hat{\mu}} \cdot \vec{u}_{\parallel}$ and $\hat{\mu}_{\perp} = \vec{\hat{\mu}} \cdot \vec{u}_{\perp}$. We then determined the averages of these components for our 13 high-quality fields. This yields $\langle \hat{\mu}_{\parallel} \rangle = 0.09 \pm 0.07$ mas yr^{-1} and $\langle \hat{\mu}_{\perp} \rangle = -0.06 \pm 0.07$ mas yr^{-1}. For comparison, the model predicts $\langle \hat{\mu}_{\parallel} \rangle = 0.08$ mas yr^{-1} and $\langle \hat{\mu}_{\perp} \rangle = 0$. Although the errors are significant, we do detect the expected sign and the expected magnitude for the rotation. This provides additional confidence in the accuracy of our results.

In our models we have assumed throughout that $di/dt = d\Theta/dt = 0$. If these terms were to have non-zero values then this would have left a signature in the residuals $\vec{\hat{\mu}}$. In particular, using model calculations similar to those in Figure 10c,d of vdM02, and assuming that the model for the internal rotation of the LMC is correct, we would have expected that in mas yr^{-1}, $\langle \hat{\mu}_{\parallel} \rangle = 0.08 - 0.046 \, d\Theta/dt$ and $\langle \hat{\mu}_{\perp} \rangle = -0.01 \, di/dt$. In these equations both $d\Theta/dt$ and di/dt are also in units of mas yr^{-1} (where 1 mas yr^{-1} = 278°/Gyr). The observed values therefore provide the following constraints on the precession and nutation of the LMC:

$$d\Theta/dt = -0.17 \pm 1.57 \text{ mas yr}^{-1} , \; di/dt = -6 \pm 7 \text{ mas yr}^{-1} . \tag{5}$$

Both quantities are consistent with zero, although the constraints are not particularly informative. The error bars are considerably larger than the precession and nutation that are expected on the basis of N-body calculations (Weinberg 2000).

5. Discussion

5.1. Comparison to Previous Proper Motion Work

We are now in a position to make comparisons with previous proper motion work. Figure 15 shows all the PM determinations to date with their 68.3% confidence ellipses. We do not include the very discrepant results of Anguita et al. (2000) and Momany & Zaggia (2005) on this plot as there must be unidentified systematic errors associated with these measurements (see discussions in Pedreros et al. 2000 and Momany & Zaggia 2005). The figure shows the region of the (μ_W, μ_N)-plane spanned by the rest of the results. These results are more-or-less consistent with each other. Our *HST* determination appears to be closest to the results of the Pedreros et al. (2002) study and the Kroupa & Bastian (1997) Hipparcos study. Our value for μ_W is on the high end of what was found in previous studies.

The measurements from all these studies can be combined to get a weighted average of the proper motion of the LMC. In doing so we first increase (as in vdM02) the error bars

of all the studies by a fixed factor so that they become statistically consistent, as judged by χ^2. The resulting grand average of all the LMC proper motion measurements is

$$\mu_W = -1.94 \pm 0.09 \text{ mas yr}^{-1}, \ \mu_N = 0.43 \pm 0.06 \text{ mas yr}^{-1} \ (HST + \text{other studies}). \quad (6)$$

In the discussion that follows we adopt the HST-only values given in equation (3).

5.2. Three-dimensional Space Motion of the LMC

The observed proper motion of the LMC quoted in equation (3) yields an estimate of its transverse velocity via

$$v_x = D_0\mu_W, \ v_y = D_0\mu_N, \quad (7)$$

where the x- and y-directions point towards the direction of West and North respectively. D_0 is the LMC distance, which we assume to be 50.1 kpc as in §4.1 (Freedman et al. 2001). This yields

$$v_x = -482 \pm 18 \text{ km s}^{-1}, \ v_y = 104 \pm 12 \text{ km s}^{-1}. \quad (8)$$

The listed errors do not include the potential contribution from the uncertainty in the distance modulus. The values of v_x and v_y correspond to a transverse velocity of $v_t = 493 \text{ km s}^{-1}$ in the direction of position angle $\Theta_t = 78°$. The systemic line-of-sight velocity is very well known from a number of different tracers including a detailed analysis of 1041 carbon stars by vdM02 who obtained $v_{sys} = 262.2 \pm 3.4 \text{ km s}^{-1}$. We are therefore in a position to ask what these measurements imply for the three-dimensional space motion of the LMC. This issue has been addressed previously by several authors but our results provide the most accurate measurement so far.

As many previous authors have done we adopt a Cartesian coordinate system (X, Y, Z) with the origin at the Galactic center, with the Z-axis pointing toward the Galactic north pole, the X-axis pointing in the direction from the Sun to the Galactic center, and the Y-axis pointing in the direction of the Sun's Galactic rotation. It is necessary to correct for the reflex motion of the Sun to determine the motion of the LMC with respect to the Milky Way. Following the equations set up in vdM02, §9.3, we get

$$\mathbf{v}_{\text{LMC}} = (-86 \pm 12, -268 \pm 11, 252 \pm 16) \text{ km s}^{-1},$$
$$v_{\text{LMC}} = 378 \pm 18 \text{ km s}^{-1},$$
$$v_{\text{LMC,rad}} = 89 \pm 4 \text{ km s}^{-1}, \ v_{\text{LMC,tan}} = 367 \pm 18 \text{ km s}^{-1}, \quad (9)$$

for the 3-D velocity of the LMC and its radial and tangential components. The fact that $v_{\text{LMC,tan}}$ is larger than the Milky Way circular velocity of $\sim 220 \text{ km s}^{-1}$ and that $v_{\text{LMC,rad}}$ is

small and positive confirms that the LMC is just past perigalacticon, as found by previous authors.

5.3. Comparison to Magellanic Stream Models

Our value for the galactocentric tangential velocity is higher than that implied by a weighted average of earlier PM measurements, which is 281 km s^{-1}. It is also a little higher than values inferred from most Magellanic Stream models. There are two main approaches to modeling the Stream, one that invokes ram-pressure stripping of MC gas by matter in the Galactic Halo, and another that invokes the tidal force of the Milky Way on the MC system. As stated in the introduction, Gardiner & Noguchi (1996) have constructed detailed simulations for the tidal distortion of the SMC owing to the Galaxy and the LMC, and get the following constraints for the motion of the LMC: $\mathbf{v}_{LMC} = (-5, -225, 194)$ km s^{-1}, $v_{LMC,rad} = 80$ km s^{-1}, and $v_{LMC,tan} = 286$ km s^{-1}. Our observed value for the tangential velocity is noticably higher, while the radial velocity seems to agree well. Our values appear more consistent with those of Heller & Rohlfs (1994) who use a combination of the tidal and ram-pressure stripping models to obtain : $\mathbf{v}_{LMC} = (-10, -287, 230)$ km s^{-1}, $v_{LMC,rad} = 107$ km s^{-1}, and $v_{LMC,tan} = 352$ km s^{-1}. The errors in the proper motion of the LMC are now technically good enough to allow distinctions between various Magellanic Stream models. Our *HST* proper motion determination for the SMC will soon follow in a subsequent paper. Taken together these two data points should provide powerful new constraints on the MC system and the gravitational potential of the Galactic Halo.

5.4. Other New Insights

Our results also lead to revised values for several other quantities that characterize the LMC. Given a revised PM we can obtain a different rotation curve $V(R)$ for the carbon stars in the LMC. This results in an amplitude of 60 km s^{-1} for the LMC rotation curve which is an increase of $\sim 20\%$ compared to the vdM02 value. This will in turn cause small changes in other estimates that are based on $V(R)$ such as the total mass of the LMC and its tidal radius.

Updated modeling of the carbon star velocity field using our revised PM values also yields an improved constraint on di/dt. Using the same methodology as in vdM02 we obtain $di/dt = -0.12 \pm 0.09$ mas yr^{-1}, which is now more consistent with zero than previously believed. This is a much stronger constraint than what we were able to obtain with the

analysis of the field-dependent PMs alone (equation (5)).

6.   Summary & Conclusions

We undertook a project using two epochs of HST/ACS data of Magellanic Cloud fields centered on background QSOs to determine the systemic proper motion of the Clouds. The LMC results are presented in this paper. We have determined the proper motion of the LMC to be $\mu_W = -2.03 \pm 0.08$ mas yr^{-1}, $\mu_N = 0.44 \pm 0.05$ mas yr^{-1}. This is accurate to better than 5%. When combined with HI data for the Magellanic Stream, this should allow improved constraints on both the mass distribution in the Galactic Halo, and theoretical models for the origin of the Magellanic Stream. Our data provides the most accurate proper motion measurement for any Milky Way satellite. In future papers, we will present results for the SMC as well as implications for the LMC-SMC system and the Magellanic Stream.

Improvements to our work may be possible by using HST with a longer baseline. A long baseline would facilitate measurements of the internal motions of the Clouds as well as an even more accurate measurement of their systemic motions. In addition we may be able to make a distance determination using the method of rotational parallax (Olling & Peterson, 2000). Rotational parallax is the method of determining distances to local group galaxies by measuring a rotation curve using both proper motions and radial velocities (see Brunthaler et al. 2005 for an application of this method to M33). Since the former are distance-dependent and the latter are not, using both methods provides a distance measurement. More generally, considerable improvement may be expected when the next generation of astrometric satellites such as SIM and $GAIA$ come on-line.

7. References

Alcock, C. 2000, Science, 287, 74

Alcock, C. et al. 2000a, ApJ, 542, 281

Alcock, C., et al. 2000b, AJ, 119, 2194

Anderson, J. & King, I. R. 2004, ACS Instrument Science Report 04-15 (Baltimore: Space Telescope Science Institute) (AK04)

Anderson, J., & King, I. R. 2003, PASP, 115, 113

Anguita, C., Loyola, P., & Pedreros, M. H. 2000, AJ, 120, 845

Bristow, P., & Alexov, A. 2002, ST-ECF Instrument Science Report CE-STIS 2002-01 (Garching bei Munchen: Space Telescope European Coordinating Facility)

Bristow, P., Piatek, S., & Pryor, C. 2005, in ST-ECF Newsletter 38, p. 12 (Garching bei Munchen: Space Telescope European Coordinating Facility)

Brüns, C., et al. 2005, A&A, 432, 45

Brunthaler, A., Reid, M. J., Falcke, H., Greenhill, L. J., & Henkel, C. 2005, Science, 307, 1440

Drake, A. J., Cook, K. H., Alcock, C., Axelrod, T. S., Geha, M., & MACHO Collaboration 2001, BAAS, 33, 1379

Dobrzycki, A., Macri, L. M., Stanek, K. Z., & Groot, P. J. 2003, AJ, 125, 1330

Dobrzycki, A., Groot, P. J., Macri, L. M., & Stanek, K. Z. 2002, ApJ, 569, L15

Fich, M. & Tremaine, S. 1991, ARA&A, 29, 409

Freedman, W. L., et al. 2001, ApJ, 553, 47

Gardiner, L. T., & Noguchi, M. 1996, MNRAS, 278, 191

Geha, M. et al. 2003, AJ, 125, 1

Heller, P. & Rohlfs, K. 1994, A&A, 291, 743

Jones, B. F., Klemola, A. R., & Lin, D. N. C. 1994, AJ, 107, 1333

Karakla, D. 2005, *HST* Primer (Baltimore: Space Telescope Science Institute)

Krist, J. 2003, ACS Instrument Science Report 03-06 (Baltimore: Space Telescope Science Institute)

Kroupa, P., Röser, S., & Bastian, U. 1994, MNRAS, 266, 412

Kroupa, P. & Bastian, U. 1997, New Astronomy, 2, 77

Lin, D. N. C., Jones, B. F., & Klemola, A. R. 1995, ApJ, 439, 652

Merrifield, M. 1992, AJ, 103, 1552

Momany, Y., & Zaggia, S. 2005, A&A, 437, 339

Mutchler, M., & Sirianni, M. 2005, ACS Instrument Science Report 2005-03 (Baltimore: Space Telescope Science Institute)

Nikolaev, S., Drake, A. J., Keller, S. C., Cook, K. H., Dalal, N., Griest, K., Welch, D. L., & Kanbur, S. M. 2004, ApJ, 601, 260

Olling, R. P. & Peterson, D. M., 2000, astro-ph/0005484

Pavlovsky, C. 2005, ACS Instrument Handbook (Baltimore: Space Telescope Science Institute)

Pedreros, M. H., Anguita, C., & Maza, J. 2002, AJ, 123, 1971

Smecker-Hane, T. A., Cole, A. A., Gallagher, J. S., & Stetson, P. B. 2002, ApJ, 566, 239

Piatek, S., Pryor, C., Bristow, P., Olszewski, E. W., Harris, H. C., Mateo, M., Minniti, D., & Tinney, C. G. 2005, AJ, 130, 95

Riess, A. 2003, ACS Instrument Science Report 2003-09 (Baltimore: Space Telescope Science Institute)

van der Marel, R. P. 2002, in 'The Shapes of Galaxies and their Halos', Natarajan P., ed., 202, 2002 (Singapore: World Scientific)

van der Marel, R. P., Alves, D. R., Hardy, E., & Suntzeff, N. B. 2002, AJ, 124, 2639 (vdM02)

Weinberg, M. D. 2000, ApJ, 532, 922

Wilkinson, M.I., & Evans, N.W. 1999, MNRAS, 310, 645

Sofue, Y., & Rubin, V. 2001, ARA&A, 39, 137

Table 1. Sample and Observations

ID	QSOname	RA (H,M,S)	DEC (deg, ', ")	V	z	epoch1 date	visit	T_{exp} F606W (min)	T_{exp} F814W (min)	ORIENTAT (deg)	epoch2 date	visit	T_{exp} F606W (min)	ORIENTAT (deg)	$\Delta time$ (yrs)
L1	68.10972.36	5 47 50.2	-67 28 1.3	16.4	1.01	2002-09-05	1	6.7	1.7	75.3	2005-04-25	1	6.7	-51.3	2.6
L2	42.860.123	4 46 11.1	-72 5 9.0	17.3	0.26	2002-09-12	2	6.7	1.7	96.4	2004-09-14	2	6.7	96.5	2.0
L3	2.5873.82	5 16 28.9	-68 37 1.8	17.4	0.46	2002-09-24	3	6.7	1.7	100.9	2004-08-11	3	6.7	59.6	1.9
L4	58.5903.69	5 16 36.8	-66 34 35.8	18.0	2.24	2002-09-22	4	6.7	1.7	99.6	2004-09-12	4	6.7	90.3	2.0
L5	13.5717.178	5 15 36.1	-70 54 0.8	18.8	1.66	2002-09-07	5	6.7	1.7	68.8	2004-08-10	5	10.1	59.0	1.9
L6	75.13376.66	6 2 34.3	-68 30 41.1	18.7	1.07	2002-10-11	6	6.7	1.7	106.9	2004-08-13	6	7.3	57.1	1.8
L7	78.5855.788	5 16 26.3	-69 48 19.0	18.6	0.63	2002-10-28	7	6.7	1.7	135.2	2004-08-10	7	7.3	58.7	1.8
L8	53.3360.344	5 0 54.0	-66 43 59.8	18.9	1.86	2002-09-03	9	6.9	1.7	90.4	2004-09-05	9	11.5	90.5	2.0
L9	17.2227.488	4 53 56.5	-69 40 35.4	19.0	0.28	2002-09-05	11	9.5	1.7	88.6	2004-09-09	11	10.1	92.3	2.0
L10	30.11301.499	5 49 41.6	-69 44 15.1	19.9	0.46	2002-09-03	12	12.0	1.7	73.5	2004-08-10	12	21.5	48.9	1.9
L11	69.12549.21	5 57 22.4	-67 13 21.5	16.8	0.14	2003-06-04	19	6.7	1.7	-15.9	2005-04-28	18	6.7	-51.4	1.9
L12	25.3469.117	5 1 46.7	-67 32 39.8	18.3	0.38	2003-06-04	20	6.7	1.7	-3.4	2004-08-18	19	6.7	69.1	1.2
L13	6.6572.268	5 20 57.0	-70 24 52.6	18.1	1.81	2003-02-16	21	6.7	1.7	-113.5	2004-08-10	20	6.7	57.8	1.5
L14	25.3712.72	5 2 53.7	-67 25 45.0	18.6	2.17	2003-06-07	24	6.7	1.7	12.1	2004-07-13	23	6.9	36.1	1.1
L15	9.5484.258	5 14 12.1	-70 20 25.8	18.5	2.32	2003-06-04	25	6.7	1.7	-5.9	2004-07-14	24	8.0	33.3	1.1
L16	53.3970.140	5 4 36.0	-66 24 15.7	18.0	2.04	2002-12-26	26	6.7	1.7	-162.3	2005-04-07	25	6.7	-59.5	2.3
L17	63.7365.151	5 25 14.4	-65 54 45.7	18.6	0.65	2003-05-08	27	6.7	1.7	-34.9	2004-07-05	26	8.8	30.3	1.2
L18	61.8199.302	5 30 26.8	-66 48 52.9	18.7	1.79	2002-12-25	29	6.7	1.7	-169.3	2004-08-10	28	9.5	64.9	1.6
L19	82.8403.551	5 31 59.7	-69 19 51.5	19.8	0.15	2003-05-20	30	8.0	1.7	-24.1	2004-07-11	29	11.6	26.1	1.1
L20	48.2620.2719	4 56 14.3	-67 39 9.0	19.3	0.26	2002-12-01	33	9.6	1.7	174.3	2005-06-04	31	12.3	-1.1	2.5
L21	5.4892.1971	5 10 32.5	-69 27 15.5	18.9	1.58	2003-06-04	40	6.7	1.7	-4.9	2004-07-18	35	9.9	38.0	1.1

Note. — The V magnitudes quoted here are from our HST data and differ from the values in Geha et al. (2003) because 1) the MACHO resolution is much worse than that of the HRC and some of the sources were considerably blended and 2) the QSOs have some intrinsic variability. Epoch 1 has program ID 9046 (Cycle 11) and epoch 2 has program ID 10130 (Cycle 13). ORIENTAT is the position angle on the sky of the detector y-axis (in degrees east of north). Redshifts are from Geha et al. (2003).

Table 2. Results

ID	$N_{sources}$	N_{master}	N_{used}[a]	PM of field as observed				LMC PM(CM) estimate			Used?
				μ_N (mas yr^{-1})	μ_W (mas yr^{-1})	$\delta\mu_N$ (mas yr^{-1})	$\delta\mu_W$ (mas yr^{-1})	μ_N (mas yr^{-1})	μ_W (mas yr^{-1})		
L1	85	35	15	0.800	-1.162	0.089	0.121	0.550	-1.334		0
L2	70	35	10	-0.274	-2.220	0.067	0.070	0.238	-2.098		0
L3	298	109	51	0.413	-1.976	0.061	0.082	0.553	-1.969		1
L4	97	48	17	0.521	-2.121	0.118	0.150	0.692	-2.218		1
L5	240	84	27	0.102	-2.054	0.097	0.086	0.234	-2.007		0
L6	41	16	7	0.983	-1.658	0.298	0.191	0.543	-1.858		1
L7	622	269	116	0.426	-2.068	0.064	0.073	0.543	-2.045		1
L8	135	49	20	-0.050	-1.961	0.058	0.081	0.329	-2.018		1
L9	213	81	42	-0.047	-2.023	0.084	0.077	0.406	-1.967		1
L10	214	52	38	0.600	-1.934	0.087	0.099	0.337	-2.014		0
L11	59	22	8	1.186	-1.089	0.187	0.352	0.827	-1.305		0
L12	153	58	20	-0.024	-2.447	0.183	0.169	0.338	-2.478		1
L13	426	163	68	1.168	-2.455	0.078	0.134	1.230	-2.441		0
L14	97	34	18	0.136	-1.837	0.225	0.174	0.484	-1.874		1
L15	340	147	46	0.573	-2.738	0.217	0.173	0.719	-2.704		0
L16	95	33	8	0.277	-1.525	0.117	0.141	0.609	-1.597		0
L17	59	25	5	1.004	-2.313	0.185	0.289	1.067	-2.449		0
L18	100	39	12	0.914	-1.779	0.128	0.133	0.897	-1.908		0
L19	486	163	89	0.844	-1.735	0.208	0.163	0.808	-1.744		1
L20	178	44	25	0.005	-1.813	0.116	0.071	0.441	-1.833		1
L21	498	210	113	0.054	-2.464	0.122	0.115	0.254	-2.434		1

[a]$N_{sources}$ refers to the number of real sources (detected in at least half of the images). N_{master} refers to the number or sources in the master-list, i.e. detected in every image in every epoch. N_{used} refers to the number of sources that are used in the final linear transformations after the PM and δPM cuts. Columns 5-8 contain the PM estimates and their errors for each field. Columns 9 & 10 contain the PM estimates for the LMC center of mass, which includes corrections for the viewing perspective and rotation effects discussed in §4.1. The last column notes if the particular field was used in our final estimate of the center of mass motion of the LMC (Equation (3)).
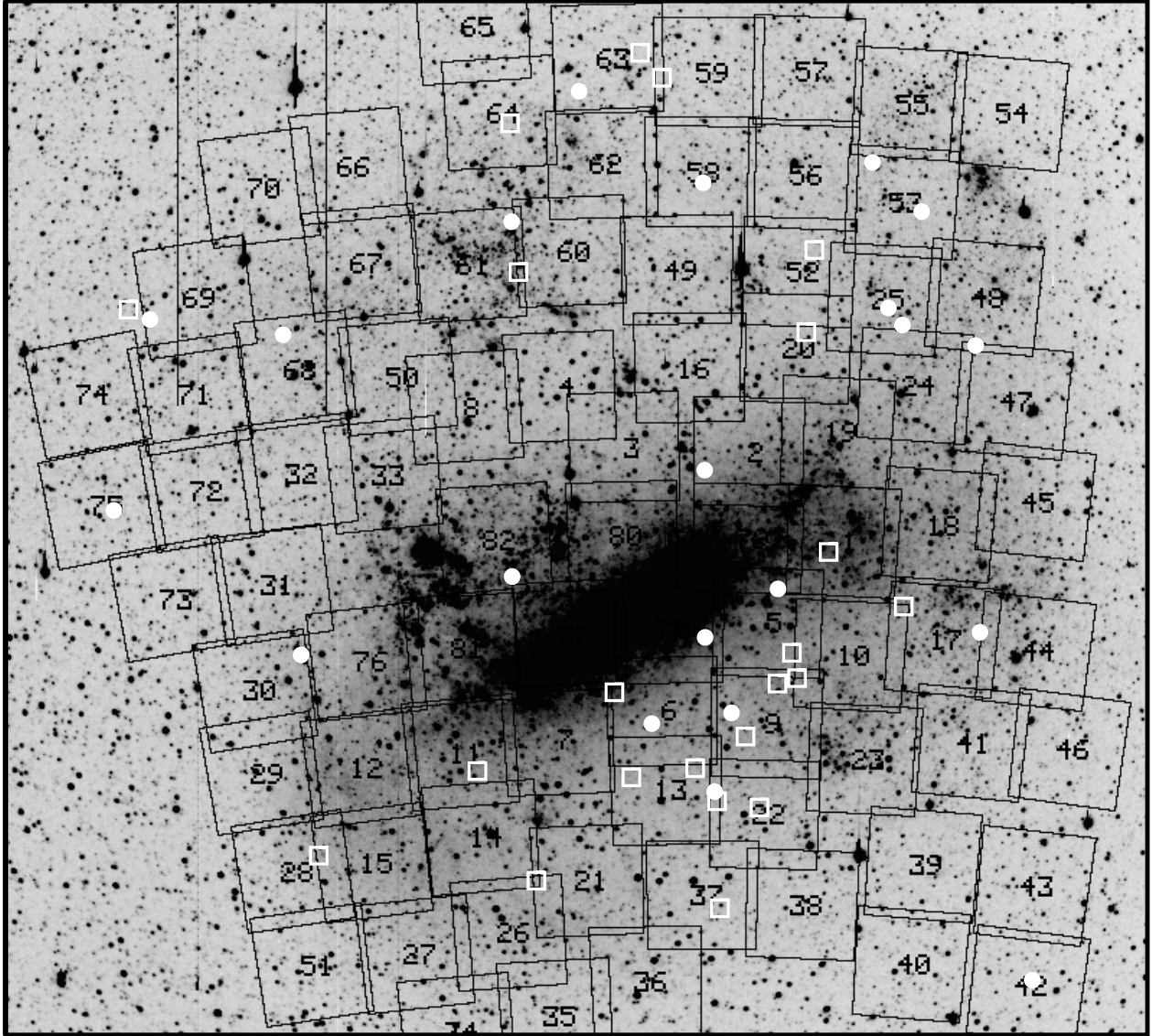
Fig. 1.— R-band image of the LMC (8° × 8°). The MACHO photometric coverage is indicated. White circles indicate reference QSOs for which we have obtained two epochs of ACS/HRC imaging and which we subsequently use in the PM analysis; squares indicate QSOs which we did propose for but for which we did not get two epochs of imaging in our snapshot program.
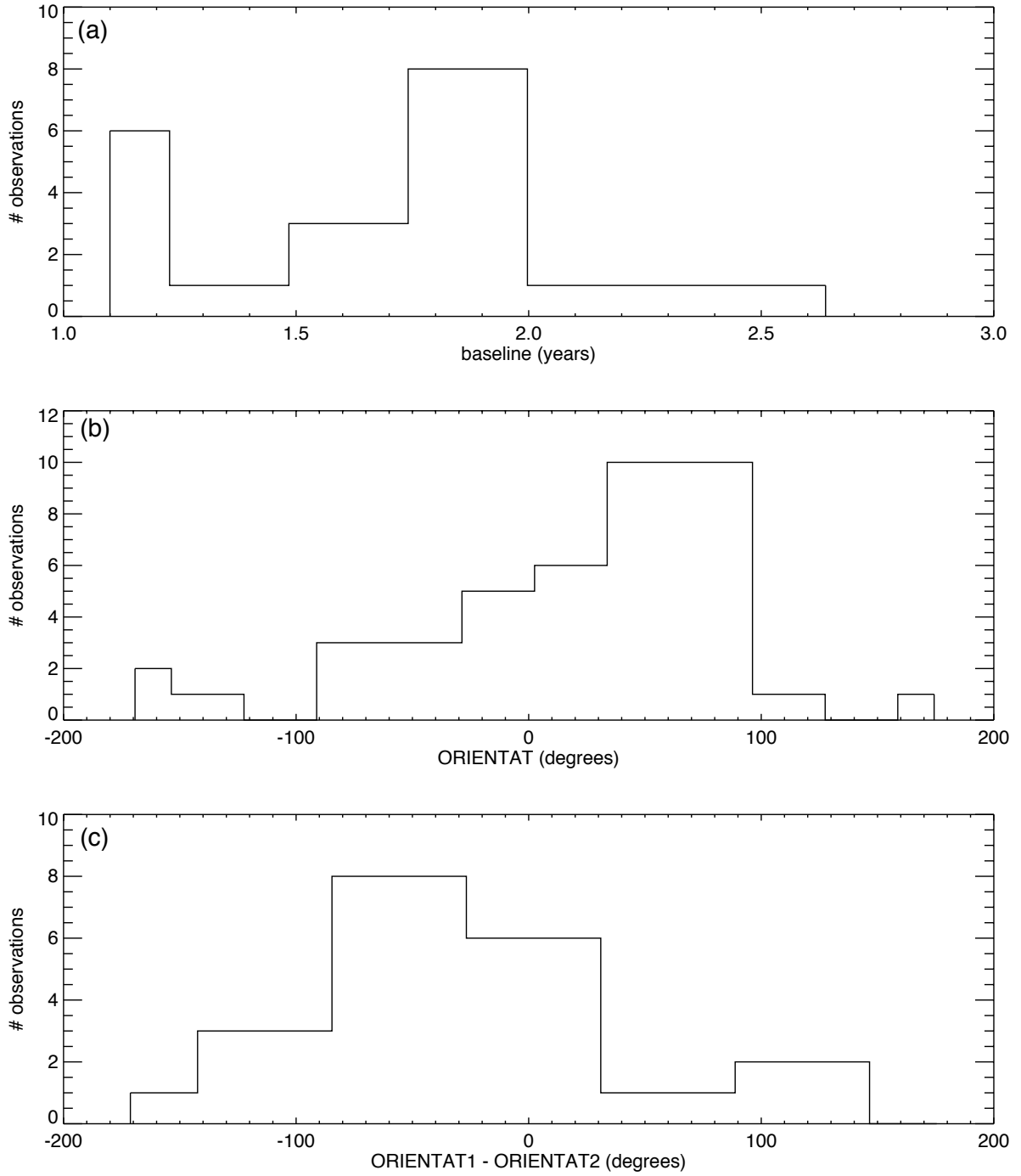
Fig. 2.— Histograms of (a) number of QSO fields with a given time baseline; (b) number of QSO fields taken with a given telescope orientation on the plane of the sky (ORIENTAT); and (c) number of fields at a given relative telescope rotation between the two epochs.
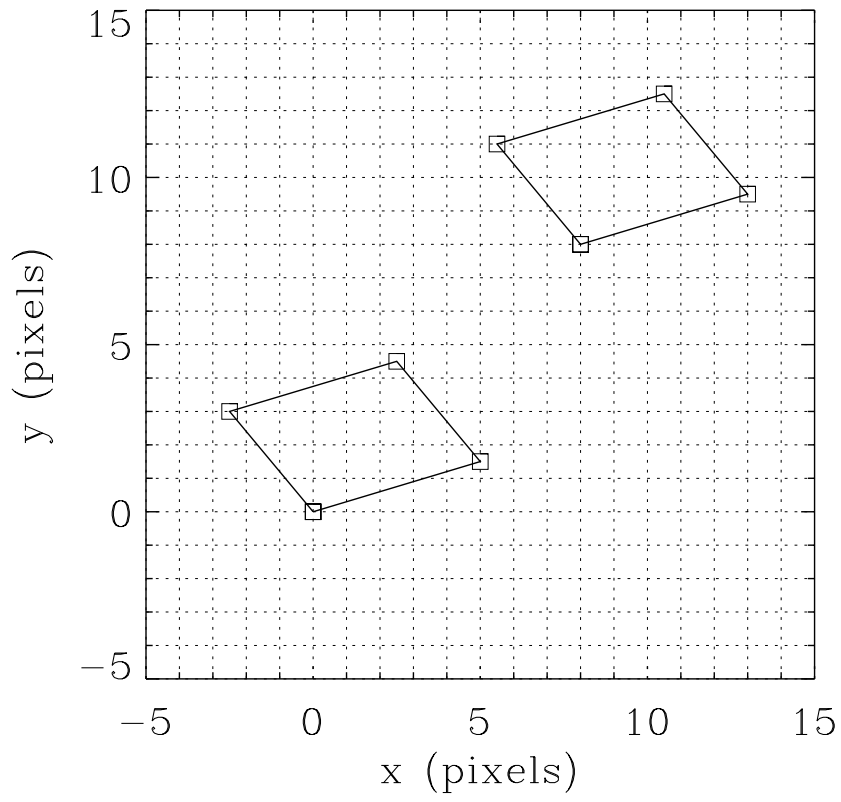
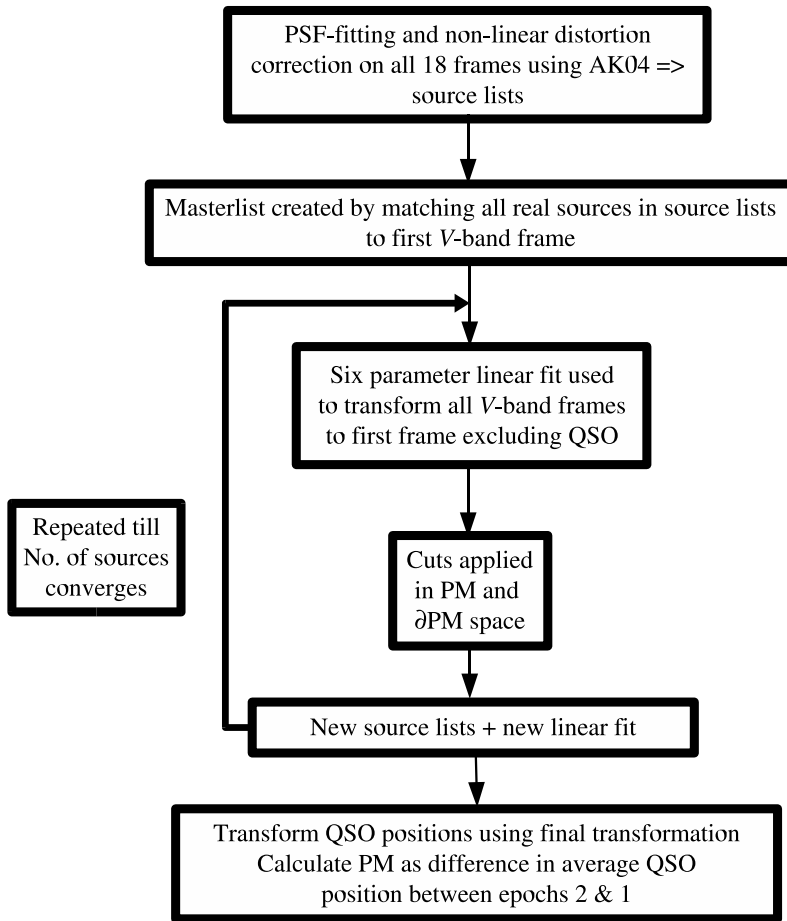Fig. 3.— The dither pattern used for the F606W images.

```
┌─────────────────────────────────────────┐
│  PSF-fitting and non-linear distortion   │
│  correction on all 18 frames using AK04 =>│
│              source lists                 │
└─────────────────────────────────────────┘
                      │
                      ▼
┌─────────────────────────────────────────┐
│ Masterlist created by matching all real  │
│    sources in source lists               │
│         to first V-band frame            │
└─────────────────────────────────────────┘
                      │
                      ▼
          ┌──────────────────────────┐
          │ Six parameter linear fit  │
          │ used to transform all     │
          │ V-band frames             │
          │ to first frame excluding  │
          │ QSO                       │
          └──────────────────────────┘
                      │
                      ▼
┌──────────────┐  ┌──────────────┐
│ Repeated till │  │ Cuts applied  │
│ No. of sources│  │ in PM and     │
│   converges   │  │ ∂PM space     │
└──────────────┘  └──────────────┘
                      │
                      ▼
┌─────────────────────────────────────────┐
│     New source lists + new linear fit    │
└─────────────────────────────────────────┘
                      │
                      ▼
┌─────────────────────────────────────────┐
│ Transform QSO positions using final      │
│ transformation                           │
│ Calculate PM as difference in average QSO │
│ position between epochs 2 & 1            │
└─────────────────────────────────────────┘
```

Fig. 4.— A flowchart outlining the steps involved in getting a PM (in pixels) for each QSO field.
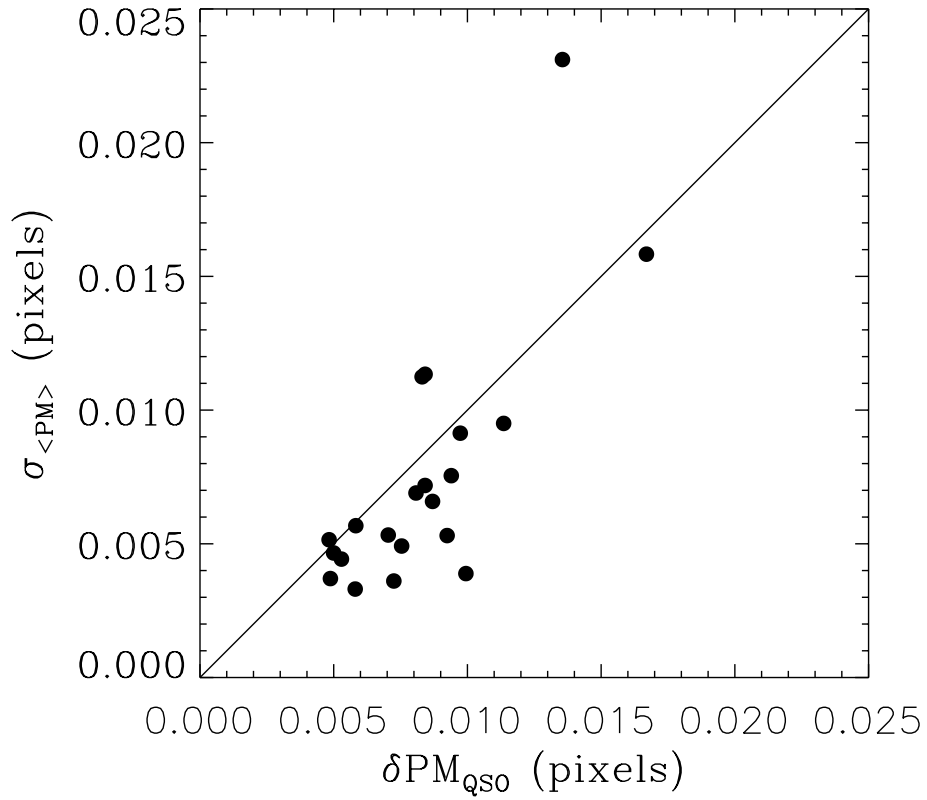
Fig. 5.— The distribution of errors in our linear transformations for each field. The x-axis shows the error in the PM of the QSO and the y-axis shows the error in the average PM of the star-field.
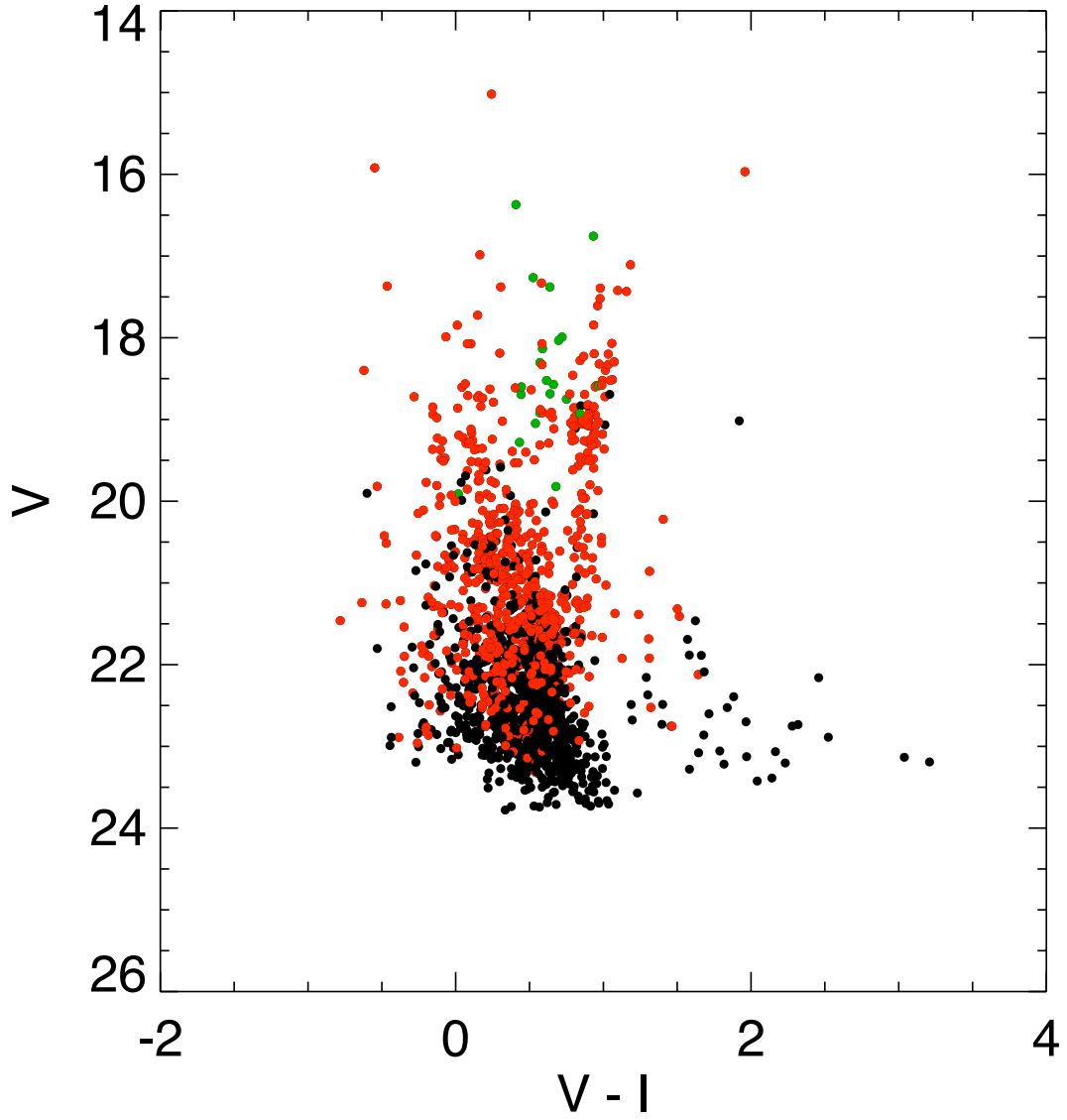
Fig. 6.— $(V - I, V)$ color-magnitude diagram for the LMC region of the sky. QSOs are marked in green, stars in the master-list with PM & δPM < 0.1 pixels are marked in red and the rest are shown in black.
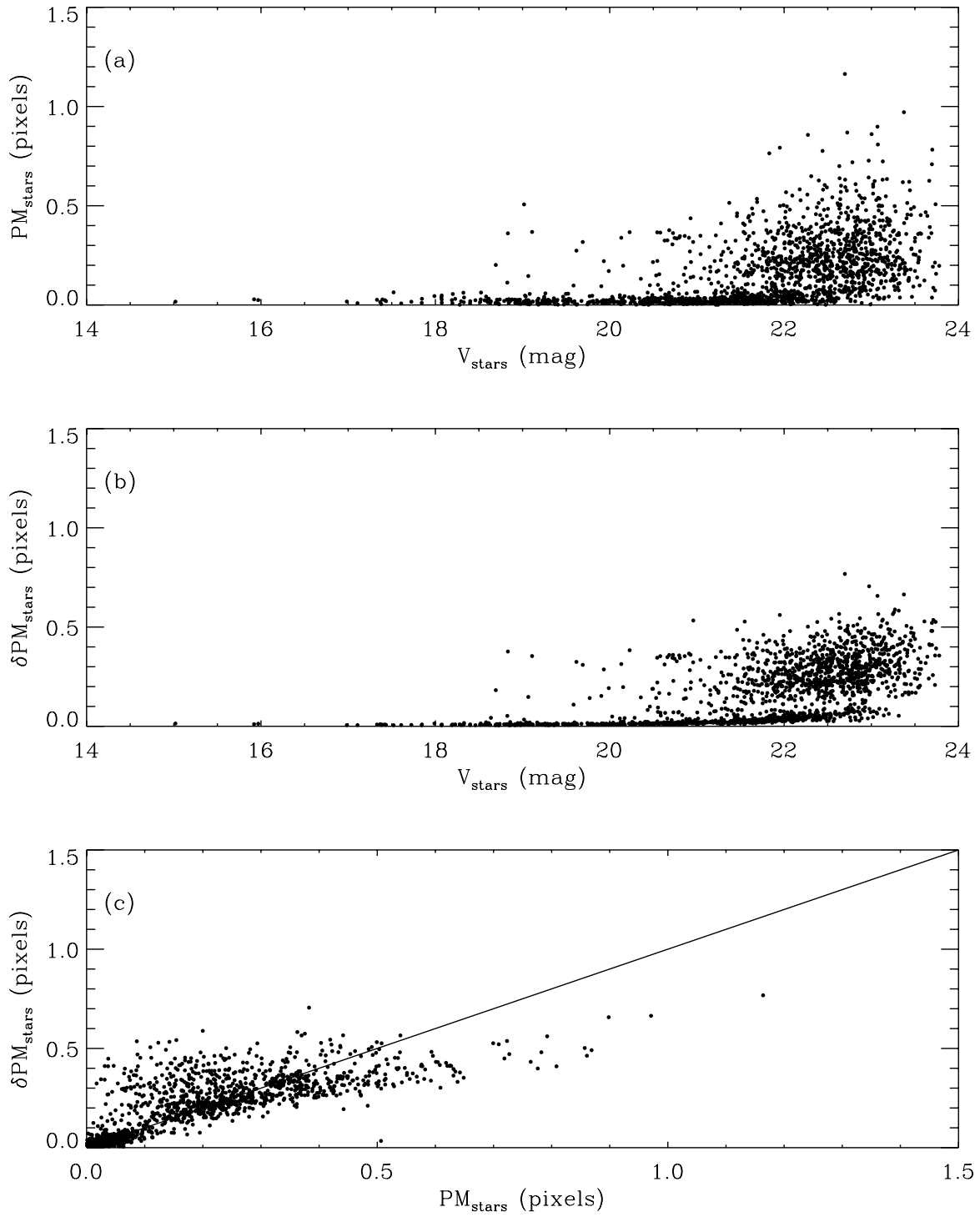
Fig. 7.— (a) PMs for all stars in all master-lists as a function of their V magnitude; (b) δPM for all stars in all master-lists as a function of V magnitude; (c) δPM vs. PM for all stars in all master-lists.
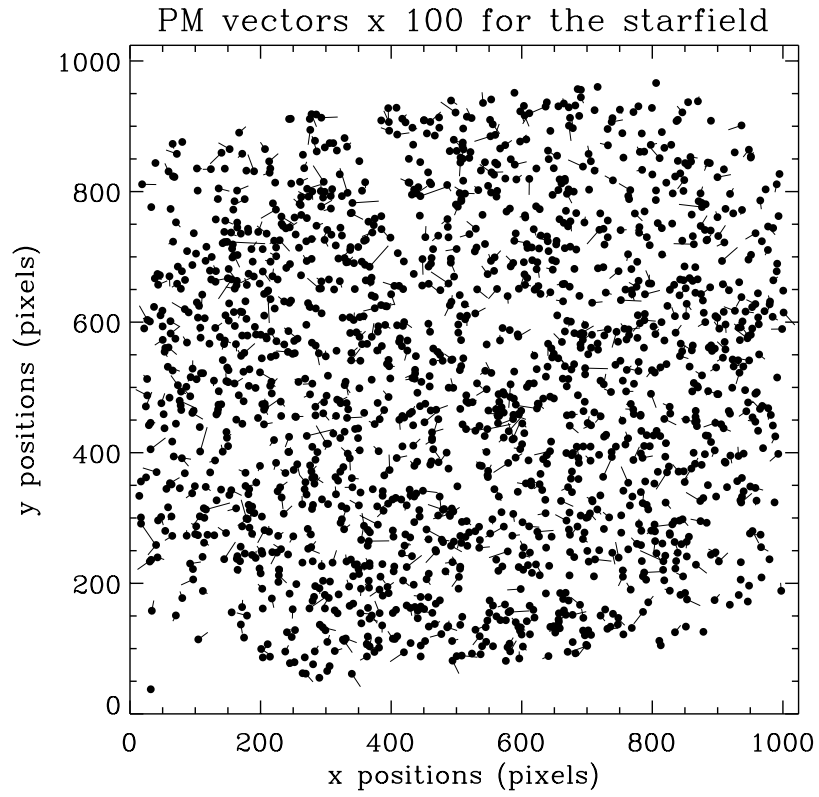
Fig. 8.— PM vectors of all stars in all master-lists magnified by a factor of 100.
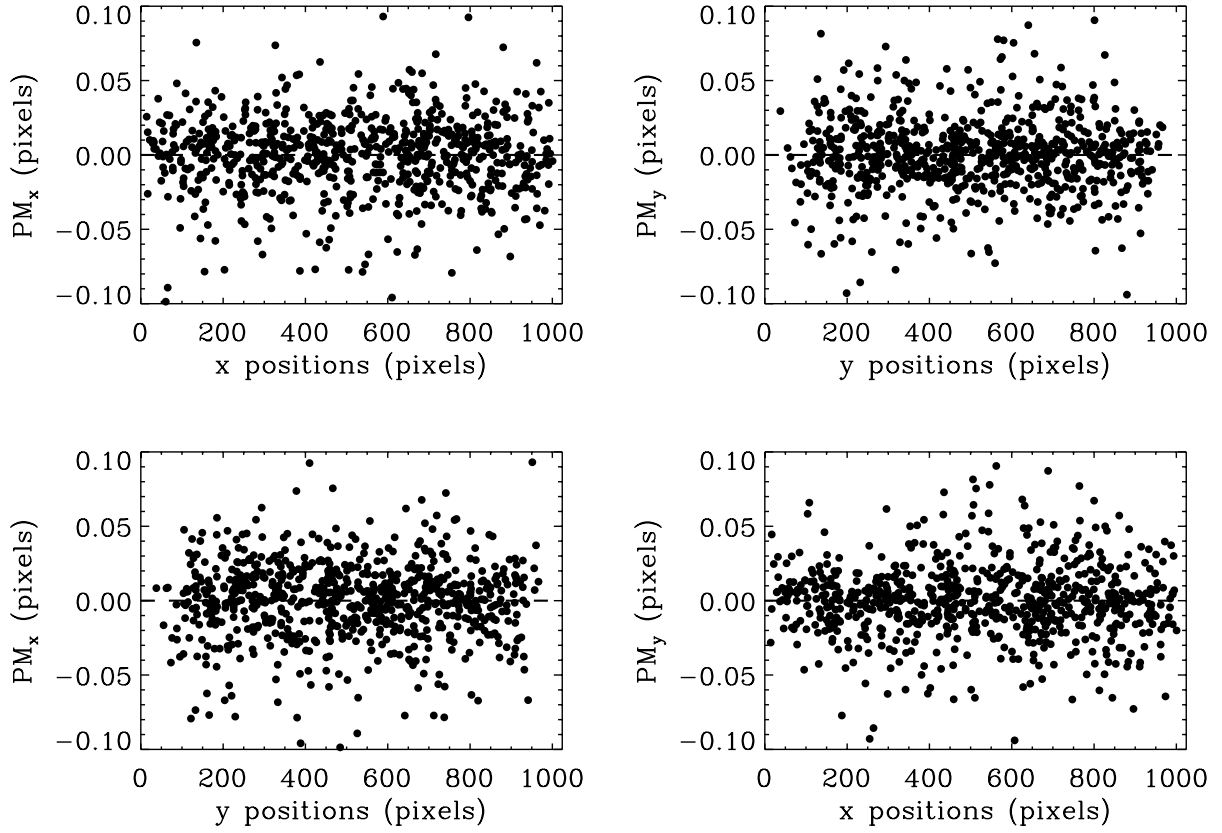
Fig. 9.— PMs of the stars in the masterlist that have PM and δPM < 0.1 pixels versus chip location separately for x and y to see if there are any systematic trends with position. These are the stars that are used in our final linear transformations.
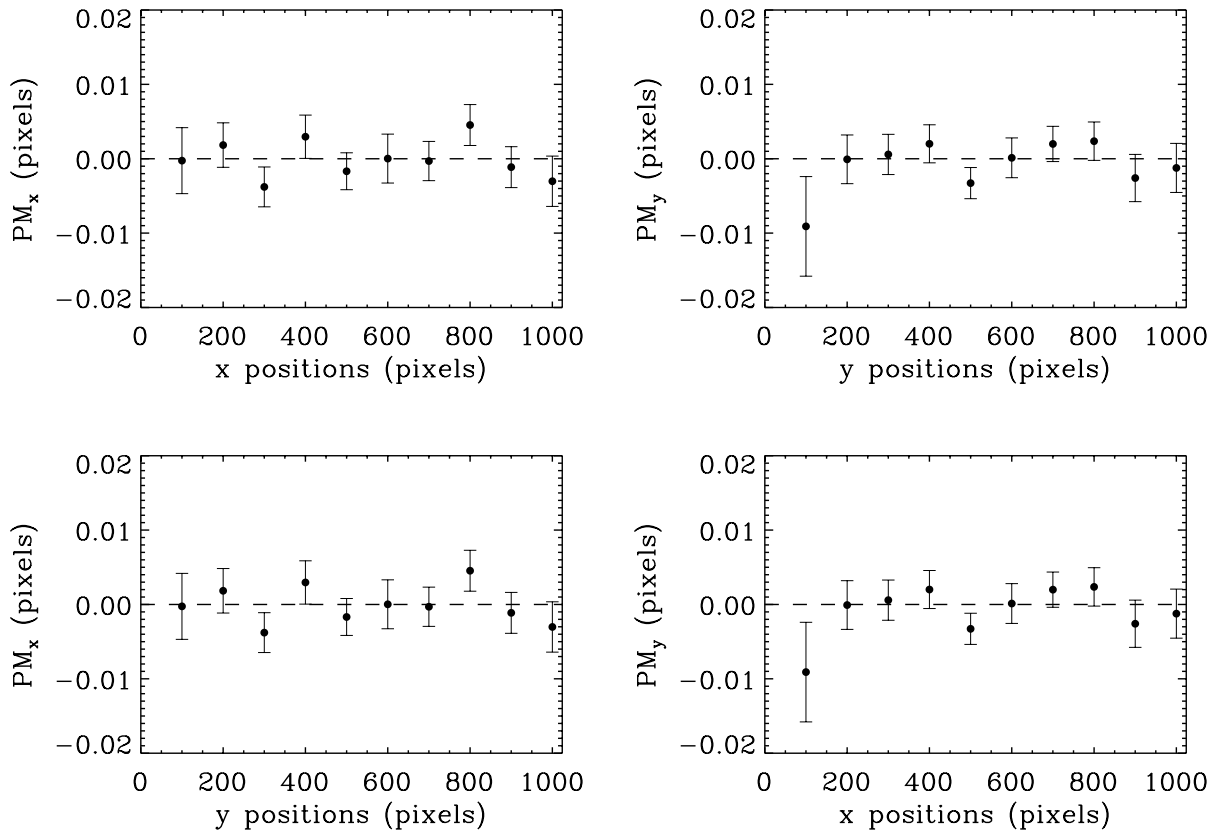
Fig. 10.— Average PMs of the stars in the masterlist that have PM and δPM < 0.1 pixels versus chip location. The PMs of the stars have been binned for every 100 pixels and then averaged.
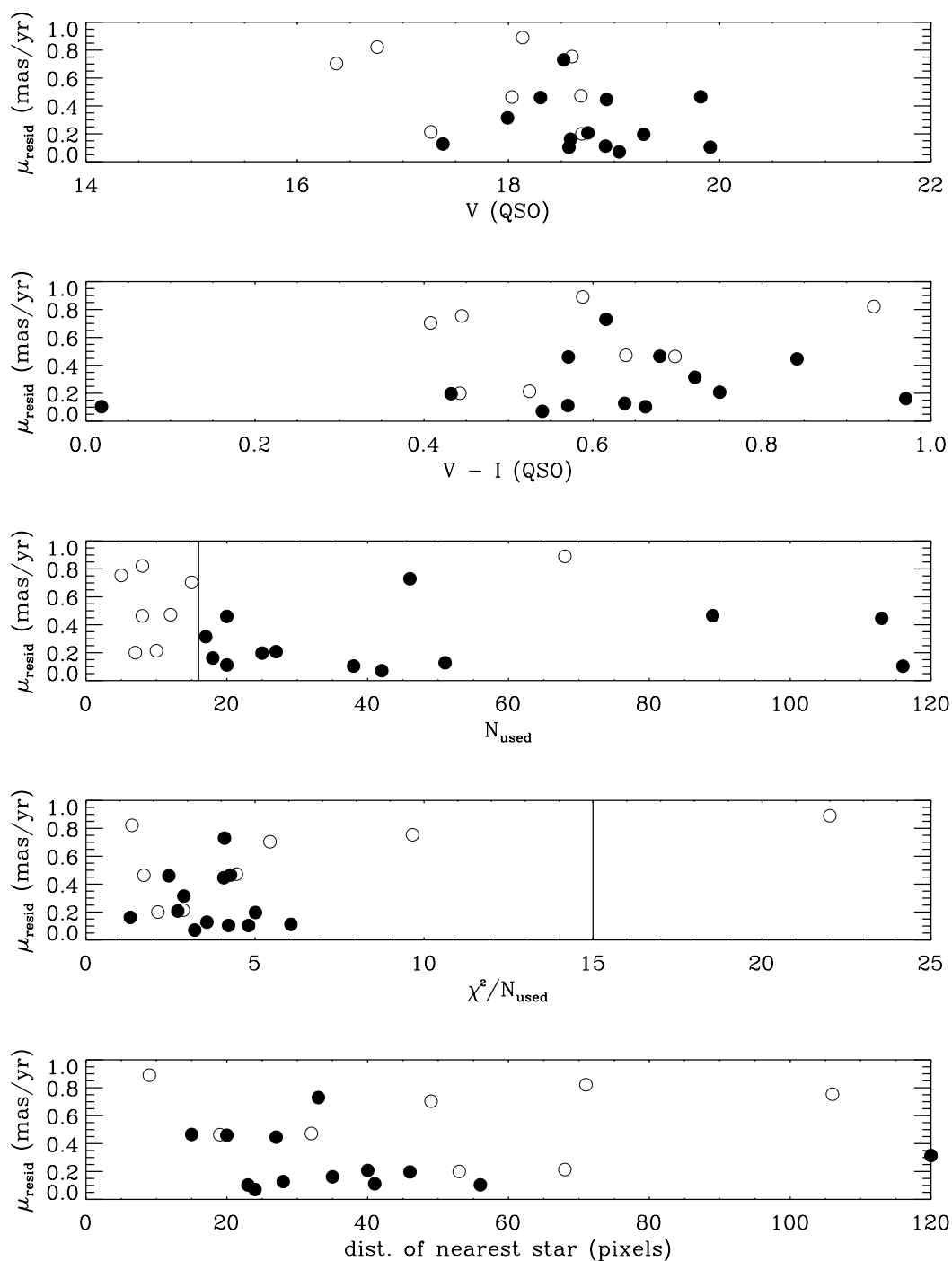
Fig. 11.— Plots of μ_{resid} as a function of QSO V magnitude, $V - I$ color, N_{used}, χ^2/N_{used} and distance to the nearest neighboring star. To select only the highest quality fields (closed circles), we retained only fields with $N_{\mathrm{used}} > 16$ and $\chi^2/N_{\mathrm{used}} < 15$ (vertical lines) in our final sample. The fields that are rejected on the basis of these cuts are shown with open circles in each panel.
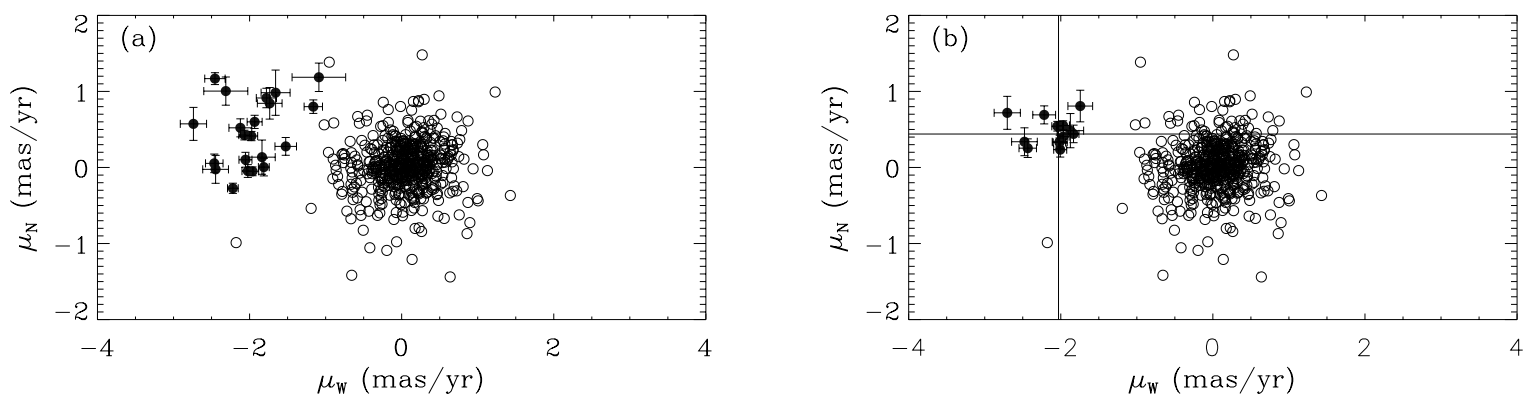
Fig. 12.— (a) The observed PM (μ_W, μ_N) for all the QSO fields (i.e., $-1 \times$ the observed reflex motion of the QSO; columns 5 & 6 of Table 2); (b) the estimates $\mathrm{PM_{est}(CM)}$ of the LMC center of mass proper motion (columns 9 & 10 of Table 2) for the 13 "high quality" fields. These include corrections for viewing perspective and internal rotation. The residual PMs of the LMC stars in all the fields are plotted with open circles in both panels. The reflex motions of the QSOs clearly separate from the star motions. The straight lines in (b) mark the weighted average of the 13 fields, as listed in equation (3).
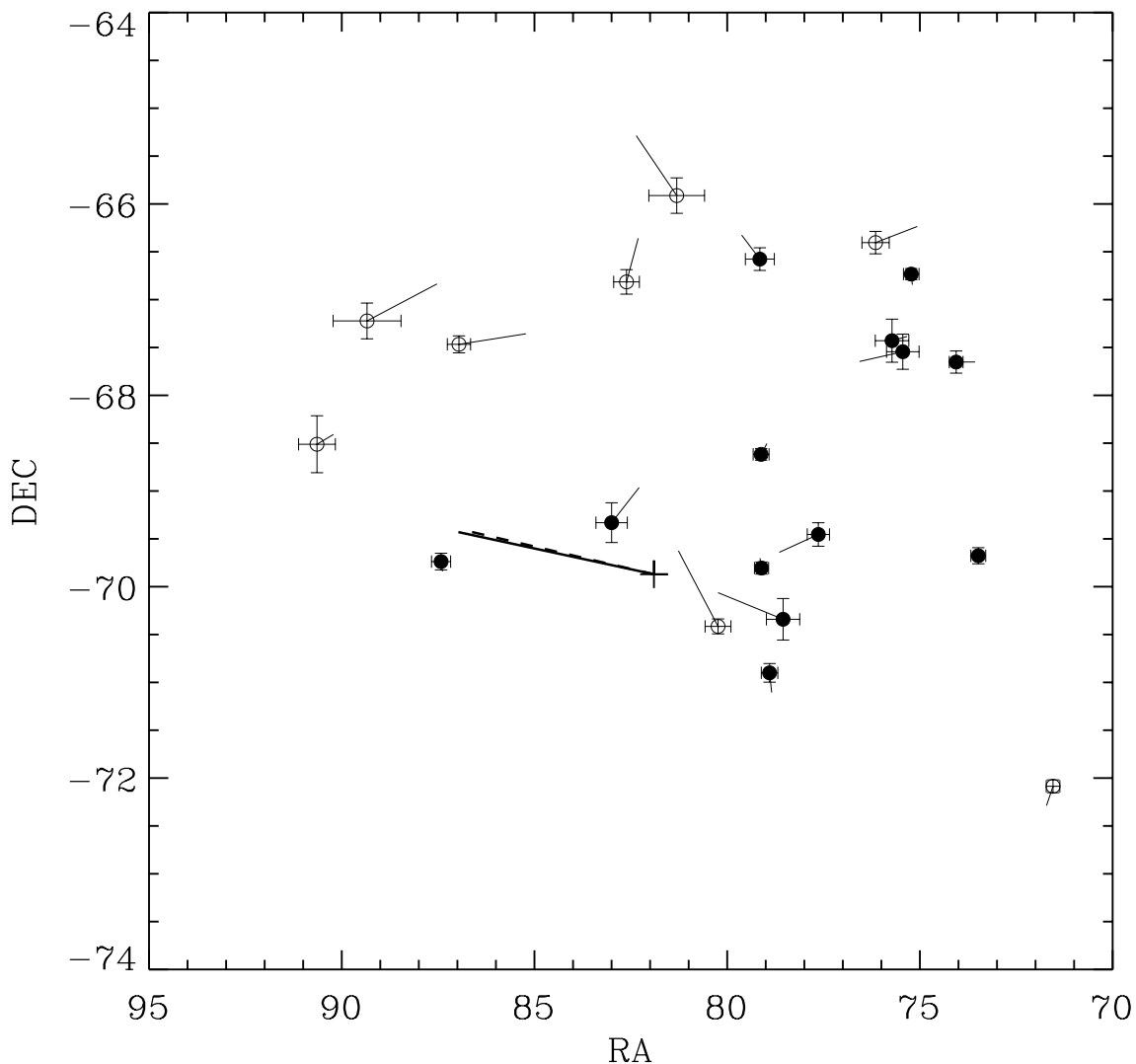
Fig. 13.— Circles show the positions of the QSO fields. The fields that are rejected (from our final LMC PM estimate) are shown with open circles and the 13 "high quality" fields are shown with filled circles. The error bars for each field are plotted as well. The vectors at these circles show the residuals between the PM estimates, $PM_{est}(CM)$, derived from the data for these fields and the adopted weighted average. The latter is given in equation (3) and is shown by the bold solid vector that is anchored by a plus sign. The dashed vector (also anchored by the plus sign) represents the straight average of all 21 fields (columns 5 & 6 of Table 2).
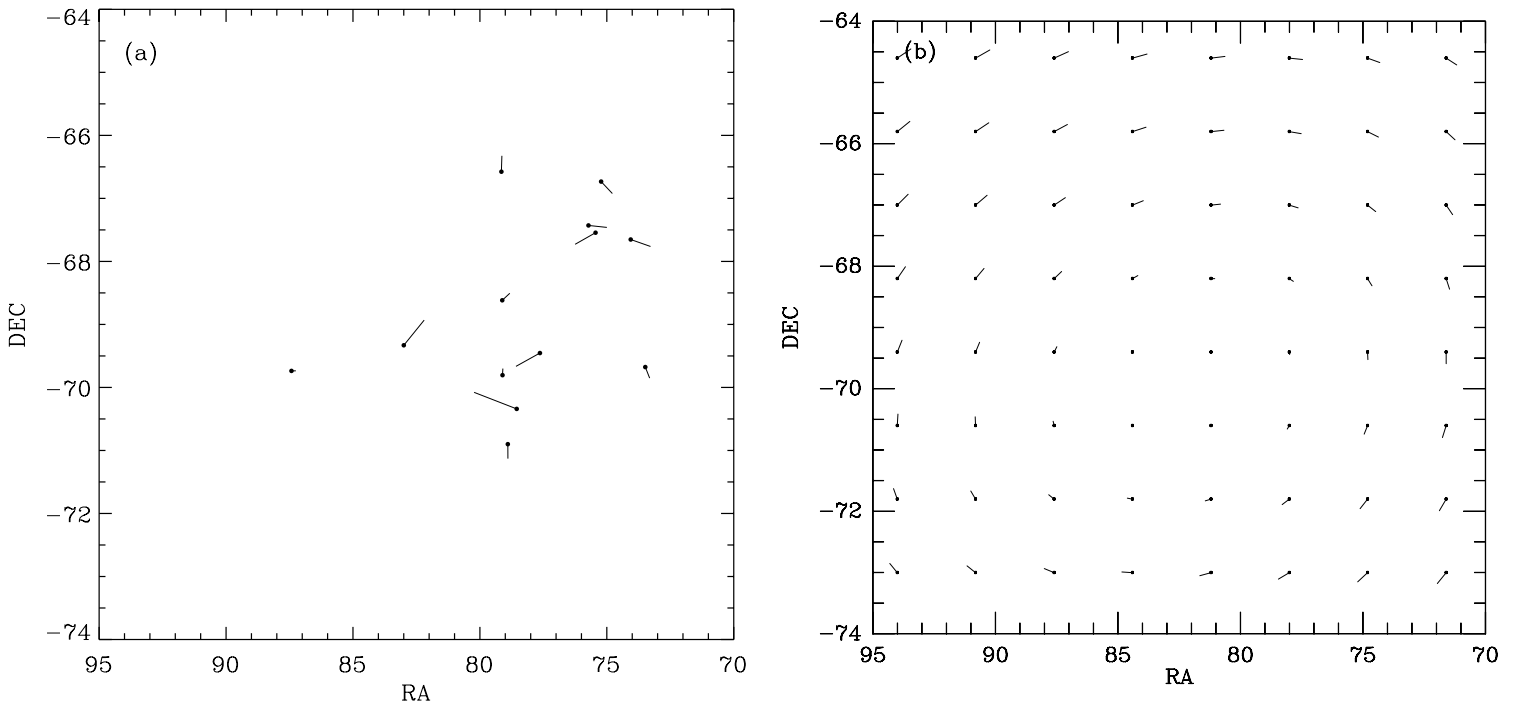
Fig. 14.— (a) LMC internal proper motion rotation estimates $\hat{\mu}_{\mathrm{resid}}$ for the high quality fields. (b) The expected rotation field of the LMC from the best fit model for the line-of-sight velocities of carbon stars described in vdM02 and §4.1.
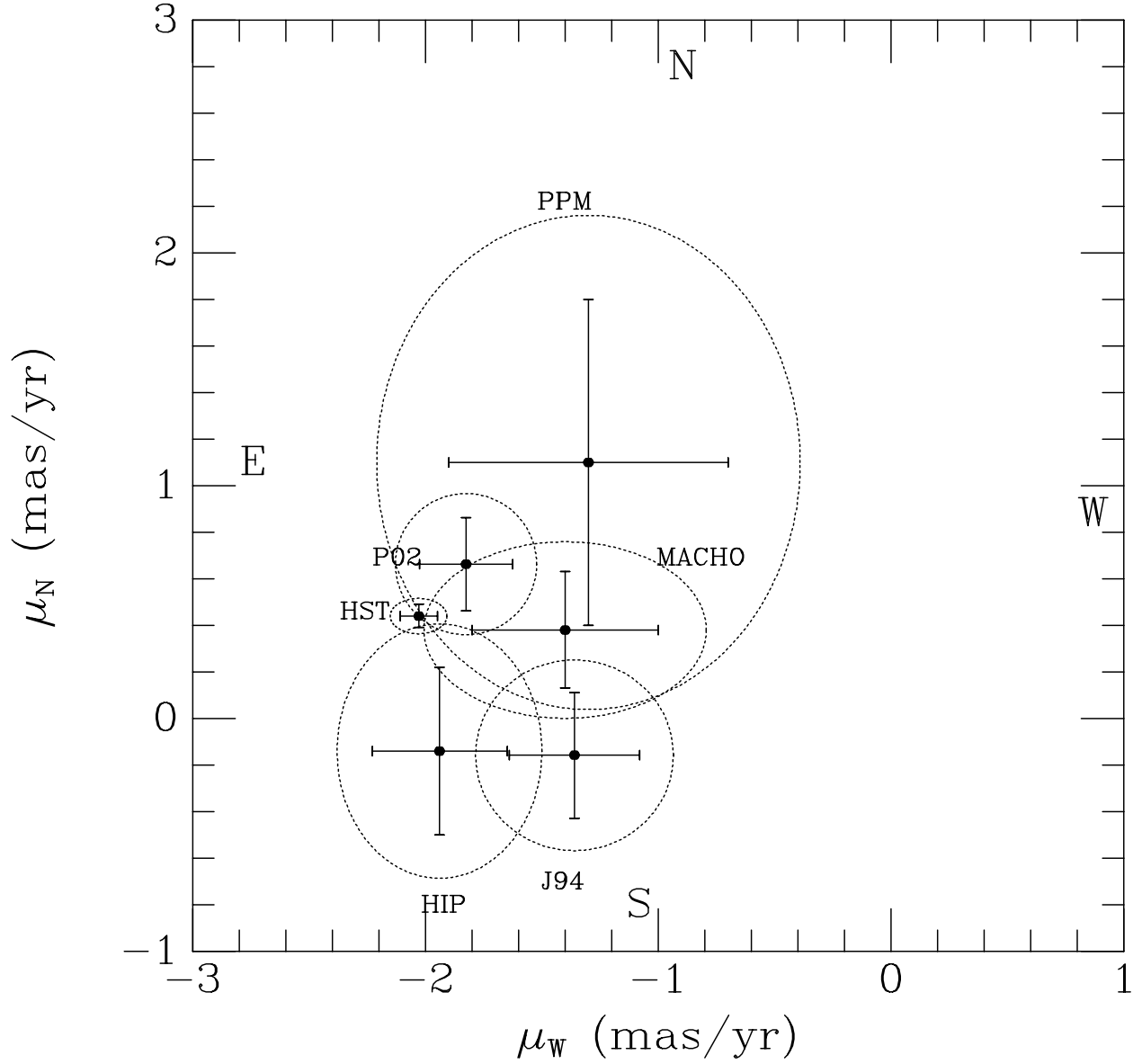
Fig. 15.— The (μ_W, μ_N)-plane spanned by the proper motion components of the LMC center of mass from various studies. Dotted ellipses are the corresponding 68.3% confidence regions. PPM stands for the Kroupa et al. (1994) study, P02 for Pedreros et al. (2002), MACHO for Drake et al. (2001), HIP for Kroupa & Bastian (1997), J94 for Jones et al. (1994), and HST for this study.